Diapycnal displacement, diffusion, and distortion of tracers in the ocean

Henri F. Drake,[a,b] Xiaozhou Ruan,[c] Raffaele Ferrari,[c]

[a] *Princeton University / Geophysical Fluid Dynamics Laboratory*

[b] *Previously, MIT–WHOI Joint Program in Oceanography/Applied Ocean Science & Engineering, Cambridge and Woods Hole, Massachusetts.*

[c] *Massachusetts Institute of Technology, Department of Earth, Atmospheric, and Planetary Sciences*

Corresponding author: Henri F. Drake, henrifdrake@gmail.com

Early Online Release: This preliminary version has been accepted for publication in *Journal of Physical Oceanography* cited, and has been assigned DOI 10.1175/JPO-D-22-0010.1. The final typeset copyedited article will replace the EOR at the above DOI when it is published.

ABSTRACT: Small-scale mixing drives the diabatic upwelling that closes the abyssal ocean overturning circulation. Indirect microstructure measurements of in-situ turbulence suggest that mixing is bottom-enhanced over rough topography, implying downwelling in the interior and stronger upwelling in a sloping bottom boundary layer. Tracer Release Experiments (TREs), in which inert tracers are purposefully released and their dispersion is surveyed over time, have been used to independently infer turbulent diffusivities—but typically provide estimates in excess of microstructure ones. In an attempt to reconcile these differences, Ruan and Ferrari (2021) derived exact tracer-weighted buoyancy moment diagnostics, which we here apply to quasi-realistic simulations. A tracer's diapycnal displacement rate is exactly twice the tracer-averaged buoyancy velocity, itself a convolution of an asymmetric upwelling/downwelling dipole. The tracer's diapycnal spreading rate, however, involves both the expected positive contribution from the tracer-averaged in-situ diffusion as well as an additional non-linear diapycnal distortion term, which is caused by correlations between buoyancy and the buoyancy velocity, and can be of either sign. Distortion is generally positive (stretching) due to bottom-enhanced mixing in the stratified interior but negative (contraction) near the bottom. Our simulations suggest that these two effects coincidentally cancel for the Brazil Basin Tracer Release Experiment, resulting in negligible net distortion. By contrast, near-bottom tracers experience leading-order distortion that varies in time. Errors in tracer moments due to realistically sparse sampling are generally small ($< 20\%$), especially compared to the $O(1)$ structural errors due to the omission of distortion effects in inverse models. These results suggest that TREs, although indispensable, should not be treated as "unambiguous" constraints on diapycnal mixing.

Accepted for publication in *Journal of Physical Oceanography*. DOI 10.1175/JPO-D-22-0010.1.

1. Introduction

The lower limb of the ocean's meridional overturning circulation traces the diabatic life cycle of abyssal bottom waters (Talley 2013), which store vast quantities of climatically-active tracers like heat and carbon. Bottom waters are formed at the surface of the Southern Ocean by atmospheric cooling and brine rejection and are consumed in the abyssal ocean by buoyancy-flux convergence due to small-scale mixing and geothermal heating (Abernathey et al. 2016; de Lavergne et al. 2016b). Since mixing processes are too small to be resolved by large-scale ocean models, the rate at which tracers are mixed across density surfaces—the diapycnal diffusivity—enters as a key free parameter in ocean and climate models (Bryan and Lewis 1979; Simmons et al. 2004; de Lavergne et al. 2020). While early models of the abyssal circulation assume this mixing to be spatially uniform (Munk 1966; Stommel and Arons 1959), subsequent in-situ observations reveal a complex geography of mixing processes (e.g. Polzin et al. 1997; Waterhouse et al. 2014). A robust pattern that emerges from these in-situ mixing observations is the bottom-enhancement of mixing over rough topography, consistent with theoretical arguments that this mixing is predominantly caused by breaking internal waves radiating from flow over topography (Munk and Wunsch 1998; Polzin 2009; Nikurashin and Ferrari 2009; Nikurashin and Legg 2011; MacKinnon et al. 2017; Whalen et al. 2020).

The observed bottom-enhancement of deep mixing demands a revision of classic abyssal circulation theory: in the stratified interior, bottom-enhanced mixing above rough topography results in a layer of buoyancy flux divergence—the downwelling Stratified Mixing Layer (SML)—and a thin layer of even larger buoyancy flux convergence at the insulating[1] seafloor—the upwelling Bottom Boundary Layer (BBL). These ideas were first introduced at the regional scale in the Brazil Basin (Polzin et al. 1997; Ledwell et al. 2000; St. Laurent et al. 2001; Huang and Jin 2002) and then generalized to the global context (Ferrari et al. 2016; de Lavergne et al. 2016b; McDougall and Ferrari 2017; Callies and Ferrari 2018): the global diabatic overturning circulation is the small residual of substantial downwelling in the SML and even larger upwelling in the BBL (Drake et al. 2020). While the existence of these upwelling/downwelling flows is virtually guaranteed by the combination of a bottom-enhanced turbulent buoyancy flux and an insulating boundary condition along a sloping seafloor, the structure, magnitude, and underlying dynamics of these flows remain

[1]Geothermal heat flux into the BBL acts to amplify upwelling, but is thought to be secondary to mixing globally (de Lavergne et al. 2016a) and is negligible in the Brazil Basin subregion considered here (Thurnherr et al. 2020).

poorly understood (see Drake 2021; Polzin and McDougall 2022). Since diapycnal (or vertical) velocities and fluxes are challenging to directly measure (and interpret—see Polzin et al. 2021 for a recent example), bulk methods, such as volume or buoyancy budgets (e.g. St. Laurent et al. 2001; Lele et al. 2021), are commonly used instead to indirectly infer the flow. Watermass transformation analysis (Walin 1982; Marshall et al. 1999) is a commonly-used framework which combines volume and buoyancy budgets to express diapycnal transport across a buoyancy surface in terms of the average turbulent buoyancy flux convergence along the surface (de Lavergne et al. 2016b; Ferrari et al. 2016), which can be inferred from indirect observations (Spingys et al. 2021).

There are several observational methods for indirectly estimating in-situ turbulent buoyancy fluxes and their corresponding diffusivities (listed roughly in order of decreasing accuracy and generality; see Gregg et al. 2018):

1. velocity shear microstructure, ϵ, based on an approximate turbulent kinetic energy budget (Osborn 1980);

2. temperature variance microstructure χ, based on an approximate temperature variance budget (Osborn and Cox 1972);

3. scaling analysis, e.g. assuming the Thorpe scale L_T of density overturns approximates the Ozmidov scale L_O (Thorpe and Deacon 1977; Dillon 1982; Mashayek et al. 2021); and

4. shear/strain variance finestructure ϵ_{IW}, based on idealized spectral models of internal wave dynamics (e.g. Garrett and Munk 1972, 1975; Henyey et al. 1986; Gregg 1989; Polzin et al. 1995; Gregg et al. 2003; Kunze et al. 2006; Dematteis and Lvov 2021)

All of these methods are indirect and require some degree of approximation to convert the measured quantity into an in-situ diffusivity (see Taylor et al. 2019), e.g. $\kappa \equiv -\frac{\langle w'b' \rangle}{\langle b_z \rangle} \simeq \frac{0.2\epsilon}{\langle b_z \rangle}$ (Osborn and Cox 1972). Furthermore, they provide only localized snapshots of spatially and temporally intermittent mixing events and thus may provide biased estimates of the *mean* diffusivity κ (Whalen 2021), which is often the goal of parameterization. How any of these estimates of vertical buoyancy fluxes or turbulent diffusivities relate to the three-dimensional divergence of the turbulent buoyancy flux (and thus the diapycnal velocity) is a major open question (Polzin and McDougall 2022).

Accepted for publication in *Journal of Physical Oceanography*. DOI 10.1175/JPO-D-22-0010.1.

Tracer (or Dye[2]) Release Experiments (TREs; Watson et al. 1988) are considered by many to provide the gold standard of mixing rate estimates. In TREs, an assumed inert chemical tracer is deliberately injected into the ocean and its distribution is surveyed by ship-board rosette sampling over timescales of months to years. The evolution of the tracer is then inverted (using approximate advection-diffusion models) to yield estimates of the mean diffusivity and velocity, which can be compared to independent in-situ turbulence measurements. Localized TREs are experimental analogues of the mathematician's Green's function approach and are thus easier to interpret than thermodynamic or biogeochemical tracers with less well known initial or boundary conditions and more complicated dynamics and mixing histories (e.g. Hogg et al. 1982; Lumpkin and Speer 2007; Trossman et al. 2020). However, the results of the TRE inversion process depend crucially upon the assumptions made to infer diffusivities from approximate advection-diffusion forward models.

Watson et al. (1988) pitch TREs in the ocean as an "unambiguous measure of the diapycnal mixing rate" since tracers average over the spatial and temporal variability that challenges the interpretation of in-situ mixing estimates. For example, Watson et al. (1988) hypothesize that the sparse sampling of log-normally[3] distributed mixing events by in-situ microstructure measurements risks systematically under-estimating mean mixing rates (Baker and Gibson 1987). Superficially, observations from two deep-ocean TREs seem to corroborate this hypothesis: tracer-based estimates of mixing rates are ubiquitously 1.5–10 times larger than co-located in-situ microstructure measurements (Ledwell et al. 2000; Watson et al. 2013; Mashayek et al. 2017). While there are *ad hoc* and site-specific explanations for each of these discrepancies, there is no consensus on how best to compare tracer-based and microstructure-based estimates (Gregg et al. 2018), nor what to make of the fact that tracer-based estimates seem to always exceed microstructure-based estimates.

Recent advances in the numerical modelling and theory of TREs provide some guidance for interpreting tracer-based estimates of mixing and comparing them to microstructure-based estimates. For example, Mashayek et al. (2017) use a realistic regional simulation to argue that the mixing inferred from the DIMES TRE (Watson et al. 2013) was an order-of-magnitude larger than the in-situ diffusivity estimated from microstructure because the average diapycnal spreading of the tracer was dominated by a small fraction of the tracer distribution that resided in regions of relatively vigorous mixing near rough topography. By deriving an exact evolution equation

[2]Fluorescent dye can be used for timescales of hours to days and can be sampled as much higher resolution with in-situ fluoremeters (e.g. Ledwell et al. 2004), or—for near-surface releases—remote sensing instruments (Sundermeyer et al. 2007).

[3]Cael and Mashayek 2021 argue that these biases may be even larger because turbulence distributions are log-skew-normal.

for the second tracer-weighted buoyancy moment, Holmes et al. (2019) confirm Mashayek et al. (2017)'s speculation that a tracer's buoyancy variance grows (in part) like the *tracer-weighted* in-situ diffusivity. Ruan and Ferrari (2021) present a more intuitive from of these equations, which allows them to clearly identify an additional "diapycnal distortion" term through which the bottom-enhancement of mixing in the SML induces "diapycnal stretching" that further accelerates the diapycnal spreading of the tracer. Holmes et al. (2019) demonstrate that this diapycnal stretching in the SML is somewhat compensated for by a "boundary suppression" (or, more generally, "diapycnal contraction") effect due to upwelling of relatively dense tracer in the sloping BBL. Since both of these analyses rely on extremely idealized models, it remains unclear to what extent diapycnal distortion affects tracers in realistic conditions (e.g. eddying three-dimensional flows over rough topography). Previous observational studies have speculated about the qualitative impacts of these distortion effects (Ledwell and Hickey 1995; Ledwell et al. 2000), but did not discuss whether their inverse models account for this distortion.

In this paper, we apply Ruan and Ferrari's (2021) tracer-weighted buoyancy moments method to quasi-realistic TRE simulations. We use these diagnostics to reinterpret the diapycnal downwelling and spreading observed in the Brazil Basin TRE (Ledwell et al. 2000 and St. Laurent et al. 2001) in the context of an emerging paradigm of bottom mixing layer control of the global abyssal circulation (Ferrari et al. 2016; McDougall and Ferrari 2017). We also provide guidance for the interpretation of past (e.g. Ledwell and Hickey 1995; Ledwell et al. 2004; Holtermann et al. 2012; Ledwell et al. 2016; Mackay et al. 2018; Visbeck et al. 2020) and future TREs in light of potentially significant diapycnal distortion.

2. Theory

We briefly review Ruan and Ferrari (2021)'s recently proposed framework for comparing tracer-based and microstructure-based mixing estimates, based on exact evolution equations for tracer moments in buoyancy space. The derivation begins with the conservation equations for tracer concentration c and buoyancy b,

$$\frac{\partial c}{\partial t} + \mathbf{u} \cdot \nabla c = \nabla \cdot (\kappa \nabla c) \tag{1}$$

$$\frac{\partial b}{\partial t} + \mathbf{u} \cdot \nabla b = \nabla \cdot (\kappa \nabla b)\,, \tag{2}$$

where $\mathbf{u}$ is the velocity vector, $\nabla = \left(\frac{\partial}{\partial x}, \frac{\partial}{\partial y}, \frac{\partial}{\partial z}\right)$ is the gradient operator, and κ is an isotropic turbulent diffusivity (assumed to be the same for all tracers). Buoyancy, tracer concentrations, and velocity have been filtered on spatial and temporal scales larger than those associated with small-scale turbulence (De Szoeke and Bennett 1993). For any filtered scalar ϕ, turbulent fluxes are parameterized as an enhanced diffusive flux $\mathbf{F}_\phi = -\kappa\nabla\phi$, where the effective turbulent diffusivity κ is assumed isotropic and much larger than the molecular diffusivity. For simplicity of exposition, we here approximate density as a linear function of temperature; thus, buoyancy b, density ρ, and temperature T are all proportional and will be used interchangeably throughout: $b \equiv -g\frac{\rho}{\rho_0} \approx g\alpha T$, where $\rho_0 = 1000\,\mathrm{kg/m^3}$ is a reference density and $\alpha = 2\times10^{-4}\,^\circ\mathrm{C}^{-1}$ is the thermal contraction coefficient.

a. Exact tracer-weighted buoyancy moment models

In his classic paper, Taylor (1922) demonstrates that half the growth rate of a one-dimensional (1D) tracer distribution's variance is exactly equal to the diffusivity acting upon it. Ruan and Ferrari (2021) generalize this theory to the case of variable diffusivity in a stably stratified fluid by considering moments in buoyancy space[4]. By cross-multiplying the passive tracer (1) and buoyancy (2) equations and integrating over a volume $\mathcal{V}$ containing the tracer (or bounded by insulating and impermeable boundaries), they derive straightforward and exact evolution equations for the first and second tracer-weighted buoyancy moments,

$$\partial_t \overline{T} \;=\; 2\overline{\omega} \quad \text{and} \tag{3}$$

$$\frac{1}{2}\partial_t \overline{(T')^2} \;=\; \overline{\kappa|\nabla T|^2} \;+\; 2\overline{\omega' T'}, \tag{4}$$

respectively, where overlines denote the tracer-weighted average, $\overline{\star} \equiv \frac{\int_\mathcal{V} \star\, c\,\mathrm{d}V}{\int_\mathcal{V} c\,\mathrm{d}V}$; primes denote variations from the tracer average, $\star' \equiv \star - \overline{\star}$; and $\omega \equiv \nabla\cdot(\kappa\nabla T)$ is the in-situ buoyancy velocity, which is the magnitude of the diapycnal velocity through buoyancy space (e.g. Marshall et al. 1999). Following Ruan and Ferrari (2021), we take the optional step of converting the buoyancy moment tendencies to more intuitive physical units by normalizing with the appropriate tracer-

[4]Holmes et al. (2019) present similar exact equations but do not recognize that all of the terms can be expressed exactly in terms of tracer-weighted averages. Furthermore, many of their manipulations rely on unnecessary assumptions (e.g. the normalization by a constant background stratification N^2 in their Section 6a) or are not applicable to our rough topography context (e.g. their discussion of boundary effects in their Section 6b).

weighted powers of the buoyancy gradient[5], yielding an effective diapycnal tracer velocity w_{Tracer} and effective diapycnal tracer diffusivity κ_{Tracer},

$$w_{\text{Tracer}} \equiv \frac{\partial_t \overline{T}}{\overline{|\nabla T|}} = \frac{2\overline{\omega}}{\overline{|\nabla T|}} \quad \text{and} \tag{5}$$

$$\kappa_{\text{Tracer}} \equiv \frac{1}{2}\frac{\partial_t \overline{(T')^2}}{\overline{|\nabla T|^2}} = \underbrace{\frac{\overline{\kappa|\nabla T|^2}}{\overline{|\nabla T|^2}}}_{\substack{\kappa_{\text{Taylor}} \\ \text{(diffusion)}}} + \underbrace{2\frac{\overline{\omega' T'}}{\overline{|\nabla T|^2}}}_{\substack{\kappa_{\omega} \\ \text{(distortion)}}} . \tag{6}$$

The primary goal of many TREs is to verify uncertain in-situ estimates of the mixing rate κ (the right-hand-sides), with more reliable in-situ measurements of T and c (the left-hand-sides). Assuming, for example, that correlations between κ and $|\nabla T|$ and between ω are T are small, we recover an equation similar to Taylor's (1922) classic result that in-situ mixing rates can be directly diagnosed from the tendencies of the two tracer-weighted buoyancy moments:

$$\overline{\kappa} \simeq \frac{1}{2}\frac{\partial_t \overline{(T')^2}}{\overline{|\nabla T|^2}}. \tag{7}$$

b. Interpreting the tracer-weighted buoyancy moments

Consider the extreme example of a dipole tracer distribution $c_{i,j}$, consisting of two infinitesimal patches of equal mass at locations $\mathbf{x}_i$ and $\mathbf{x}_j$,

$$c_{i,j}(\mathbf{x}) = \frac{\delta(\mathbf{x}_i) + \delta(\mathbf{x}_j)}{2}, \tag{8}$$

where $\delta(\mathbf{x})$ is the Delta function and the entire tracer distribution has unit mass, $\int_{\mathcal{V}} c \, \mathrm{d}V = 1$. Evaluating the terms in the tracer-weighted first buoyancy moment evolution equation (3) for this hypothetical tracer distribution (8), we find that the tracer warms on average at a rate of twice the average buoyancy velocity of the two patches,

$$\partial_t \overline{T} = 2\overline{\omega} = \omega_i + \omega_j, \tag{9}$$

[5]Unlike Ruan and Ferrari (2021), we do not approximate the buoyancy gradients by ignoring horizontal components, so our equations are exact.

where we use the shorthand $\phi_k \equiv \phi(\mathbf{x}_k)$. The tendency of the tracer's centered second buoyancy moment (4) is, after some algebra (e.g. expanding and refactoring terms with $\phi_i' = \phi_i - \overline{\phi} = \overline{\phi} - \phi_j$),

$$\frac{1}{2}\partial_t \overline{(T')^2} = \overline{\kappa |\nabla T|^2} + \frac{1}{2}\Delta\omega\Delta T, \tag{10}$$

where $\Delta\omega \equiv \omega_j - \omega_i$ and $\Delta T \equiv T_j - T_i$ are buoyancy velocity and temperature differences between the two patches, respectively. While the first moment tendency is simply given by the average of the two patches' tendencies, the centered second moment tendency includes an additional non-linear distortion term. If the warmer patch upwells faster than the colder patch ($\Delta\omega\Delta T > 0$), this term drives diapycnal stretching (e.g. $c_{1,3}$ and $c_{3,2}$ in Figure 1); conversely, $\Delta\omega\Delta T < 0$ corresponds to diapycnal contraction (e.g. $c_{1,2}$ in Figure 1).

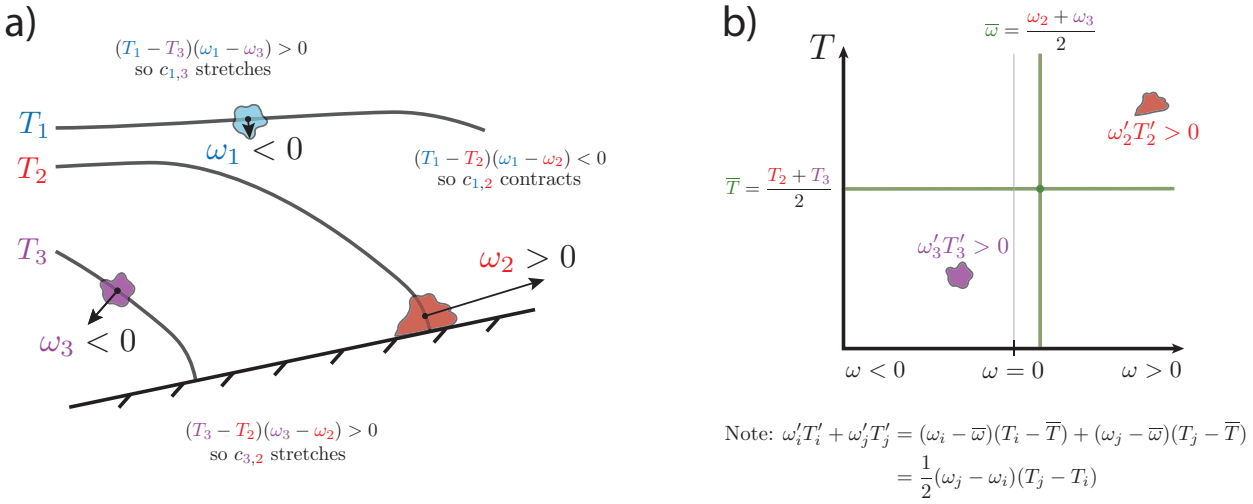

FIG. 1. Examples of diapycnal distortion of idealized dipole tracer distributions (eq. 8) in physical space (a) and in (ω, T) space (b), motivated by the quasi-realistic simulation results in Section 4. a) The three tracer distributions $c_{1,3}$, $c_{1,2}$, and $c_{3,2}$ experience diapycnal stretching or contraction effects due to temperature and buoyancy velocity differences. Gray lines show the equally-spaced temperature surfaces corresponding to the three tracer patches. Arrows represent the magnitude of the buoyancy velocity ω and are oriented normal to temperature surfaces. b) PDF of contributions to $c_{3,2}$'s net diapycnal distortion effects for both tracer patches (see Section 4d). Olive lines mark the average buoyancy velocity and temperature of the tracer.

A corollary of (10) is the fact that estimates of the in-situ diffusivity are most reliable when the injected tracer distribution is compact in buoyancy space (i.e. small ΔT), lending support to the

practice of making tracer injections as compact in buoyancy space as possible. Even for an initially compact tracer injection with small $\Delta\omega\Delta T$, however, diapycnal distortion may become significant over time as ΔT increases due to diapycnal diffusion. On the other hand, while isopycnal stirring does not increase ΔT (by definition), it can increase $\Delta\omega$ by distributing tracer into regions with varying buoyancy velocities (see Holmes et al. 2019). While the former effect is likely to be well represented in 1D advection-diffusion models used to interpret TRE data, the latter is not.

3. Numerical methods overview: simulated Tracer Release Experiments (TREs)

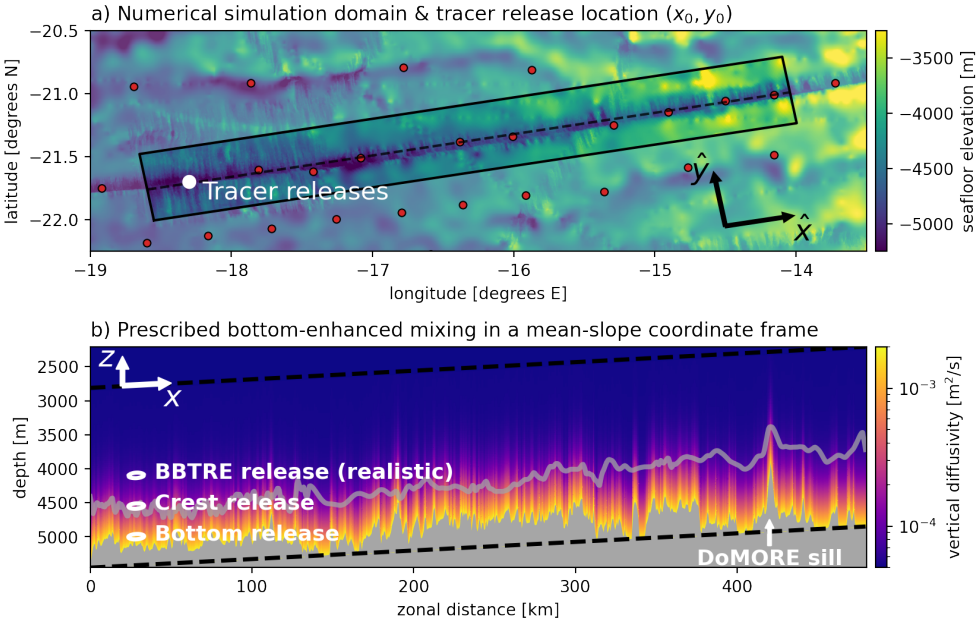

FIG. 2. Numerical model configuration: domain geometry, prescribed forcing, and key features. a) Rectangular domain (solid lines) centered along the BBTRE canyon thalweg (dashed line) and interpolated onto locally-tangent cartesian coordinates $(\hat{x}, \hat{y})$. Red dots mark the stations where the BBTRE tracer was sampled. b) Prescribed bottom-enhanced mixing (colors) along the canyon thalweg (grey shading). Dashed black lines show the domain limits in the slope-native coordinate frame (x, z). The transparent grey line shows the average height of the canyon crests, which rise 500 m to 1000 m above the thalweg (its deepest section). White dots/contours show the locations of the simulated tracer releases. The location of the prominent Dynamics of the Mid-Ocean Ridge Experiment (DoMORE–see Clément et al. 2017) sill is shown for reference.

We configure the MITgcm to simulate mixing-driven flow in the Brazil Basin TRE (BBTRE) region (Figure 2a). Inspired by sloping bottom boundary layer theory (reviewed by Garrett et al.

1993), the system is solved in a coordinate frame aligned with the mean Mid-Atlantic Ridge slope, as described in detail in a submitted companion manuscript (Drake et al. 2022) and summarized in Appendix A. The simulation is forced only by bottom-enhanced turbulent mixing, which controls diabatic tracer upwelling and spreading and is thought to provide much of the energy that drives sub-inertial abyssal flows. We impose a turbulent diffusivity κ that increases exponentially towards the seafloor at $z = -d(x, y)$ (Figure 2b),

$$\kappa(x, y, z) = \kappa(z; d) = \kappa_{\mathrm{BG}} + \kappa_{\mathrm{BOT}} \exp\left(\frac{z - d}{h}\right),$$

with parameters fit to the mean height-above-bottom microstructure profile in the region according to Callies (2018): $\kappa_{\mathrm{BOT}} = 1.8 \times 10^{-3}\,\mathrm{m}^2/\mathrm{s}$, $\kappa_{\mathrm{BG}} = 5.2 \times 10^{-5}\,\mathrm{m}^2/\mathrm{s}$, and $h = 230\,\mathrm{m}$.

After spinning up the flow to a quasi-equilibrium state at $t = 5000$ days, we release three relatively small Gaussian blobs of tracer,

$$c_n(x, y, z, t = 0) = c_0 \exp\left\{-\left(\frac{(x - x_0)^2}{2\sigma_x^2} + \frac{(y - y_0)^2}{2\sigma_y^2} + \frac{(z - z_n)^2}{2\sigma_z^2}\right)\right\}, \tag{11}$$

with horizontal widths of $\sigma_x = \sigma_y = 3.5\,\mathrm{km}$, a thickness $\sigma_z = 28\,\mathrm{m}$, and horizontal release coordinates (x_0, y_0) corresponding to the location where the tracer was released in the BBTRE ($18.3\,^\circ\mathrm{W}, 21.7\,^\circ\mathrm{S}$) (Figure 2). The tracers are released at three different heights z_n corresponding to distinct dynamically interesting regimes: far above the topography, $z_{\mathrm{BBTRE}} + d(x_0, y_0) = 1050\,\mathrm{m}$ above the seafloor (actual BBTRE release location; hereafter the BBTRE tracer); roughly at the height of the canyon crests, $z_{\mathrm{Crest}} + d(x_0, y_0) = 600\,\mathrm{m}$ (Crest); and within the thick BBL of the canyon trough, $z_{\mathrm{Bottom}} + d(x_0, y_0) = 150\,\mathrm{m}$ (Bottom). We follow the evolution of these released tracers until $t_f = 440$ days after release, roughly corresponding to the first survey in the BBTRE at 14 months.

4. Results

a. Temporal evolution of the released tracer distributions

Within the first few eddy turnover timescales, the released tracer blobs are stirred into a web of filaments along isopycnals by submesoscale eddies (Figure 3). While the BBTRE and Crest tracers

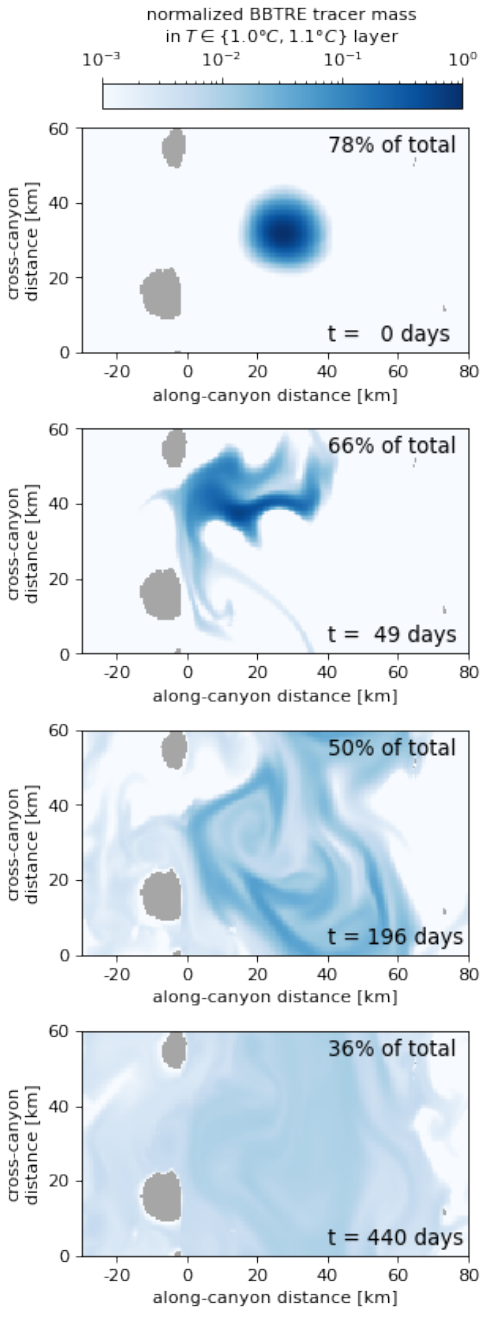

FIG. 3. Instantaneous snapshots of the BBTRE tracer mass, vertically-integrated over the {1.0 °C, 1.1 °C} temperature layer, and normalized by the maximum initial tracer mass. The fraction of the total tracer mass that remains in this layer is noted in the top right corner. The grey shading represents two major topographic obstacles, where the temperature layer intersects with the seafloor.

are released well above the canyon thalweg (its deepest section; Figure 2a), vigorous along-ridge mean flows (Figure 4) and isopycnal stirring by submesoscale eddies spread them to shallower regions (Figure 5). Spreading rates in the up-canyon direction, over the length of the experiments, are $K^{(x)} \equiv \frac{1}{2}\frac{\Delta\overline{(x')^2}}{\Delta t} \simeq 10\,\mathrm{m}^2/\mathrm{s}$ for the BBTRE tracer—the sequence of snapshots in Figure 3 suggests this is largely due to submesoscale eddy stirring. The Bottom and Crest releases experienced more rapid spreading of $O(30\,\mathrm{m}^2/\mathrm{s})$, likely due to the additional shear dispersion (Taylor 1953) by the bi-directional along-canyon mean flows (Figure 5i,j).

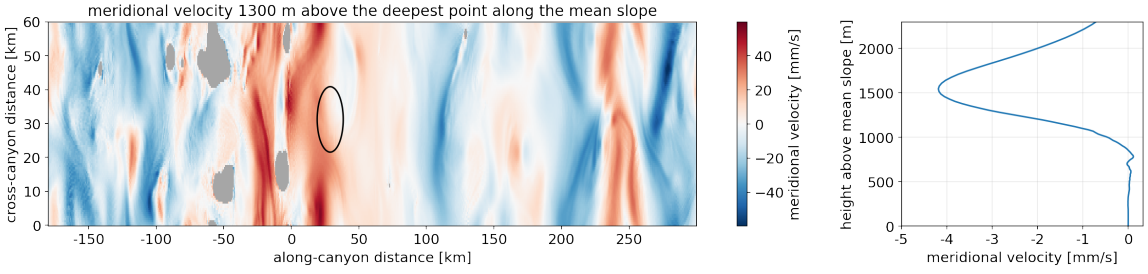

FIG. 4. (a) Cross-canyon (quasi-meridional) velocity v, 1300 m above the mean slope, i.e. at the release height of the BBTRE tracer. The black contour shows the initial extent of the tracers, which is released in an anomalously northward flow. (b) Same as a), but averaged across the whole domain.

The tracers are diffused diapycnally by the prescribed bottom-enhanced turbulent mixing (e.g. Figure 5b,d). For the BBTRE tracer, which mostly remains well above the bottom, its distribution in temperature space remains reasonably Gaussian (Figure 5d), reminiscent of diffusion with a constant diffusivity and in the absence of boundaries. For the Crest and Bottom tracers, however, the tracer distributions depart significantly from Gaussianity (Figure 5h,l), suggesting the importance of variations in the diffusivity or boundary effects (Holmes et al. 2019). Most notably, the Bottom tracer develops a bi-modal distribution in temperature space as some of the tracer spills over the minor sill at $x = 120\,\mathrm{km}$ and crosses the $T = 0.7\,^\circ\mathrm{C}$ surface (Figure 5j, l). By the end of the experiment at 440 days, most of the Bottom tracer has spilled over the sill and its bi-modal distribution collapses onto a single, warmer peak. While only the Bottom tracer exhibits a tracer-weighted diapycnal displacement that is discernible by visually inspecting the tracer distributions in temperature space, the BBTRE and Crest tracers do exhibit slow mean diapycnal downwelling and upwelling, respectively.

b. Diapycnal interior downwelling and boundary upwelling driven by bottom-enhanced mixing

As described in Section 2a, the tracer's center of mass $\overline{T}$ is displaced at a rate of *twice* the tracer-weighted buoyancy velocity $\overline{\omega} \equiv \overline{\nabla \cdot (\kappa \nabla T)}$ (eq. 3); the factor of two[6] arises because buoyancy diffuses through tracer space in addition to tracer diffusing through buoyancy space (Ruan and Ferrari 2021). Well above the seafloor, the bottom-enhancement of the diffusivity κ dominates the buoyancy velocity, resulting in diapycnal downwelling, $\omega < 0$, in a layer we thus define as the Stratified Mixing Layer (SML). Closer to the seafloor, the temperature flux must vanish to satisfy the insulating bottom boundary condition, i.e. $\mathbf{n} \cdot (-\kappa \nabla T) = 0$ where $\mathbf{n}$ is normal to the boundary, resulting in vigorous diapycnal upwelling, $\omega > 0$, in a layer we define as the Bottom Boundary Layer (BBL; see Ferrari et al. 2016).

The BBTRE tracer, which is released in the SML, exhibits diapycnal downwelling throughout the experiment (Figure 6b), consistent with the above phenomenology. The magnitude of downwelling, however, is modulated by a 45-day damped oscillation due to along-ridge advection by a mean-flow of speed $U \approx 15\,\mathrm{mm/s}$ (Figure 4a) across a periodic domain of width $L_y = 60\,\mathrm{km}$. Following a depth surface, the bulk of the tracer thus aliases the canyon's trough-crest topography on a timescale of $\tau = L_y/U \approx 45\,\mathrm{days}$, oscillating between weak diapycnal downwelling when well above the canyon floor and, because of the bottom-enhanced diffusivity profiles, exponentially stronger downwelling when it passes over the shallower hills surrounding the canyon. This modulation is damped over time as the tracer spreads isopycnally and spans a region wider than the typical trough-crest separation (Figure 5a).

[6]Ledwell et al. (1998) attempt to compare an estimate of the left-hand-side of (5) from a TRE with an estimate of the right-hand-side based on St. Laurent and Schmitt's (1999) microstructure analysis; however, they appear to have erroneously omitted the factor of two in the first moment equation (5), which would have made the two estimates even more consistent. This example highlights the importance of rigorously deriving the physical models used to interpret TRE observations.

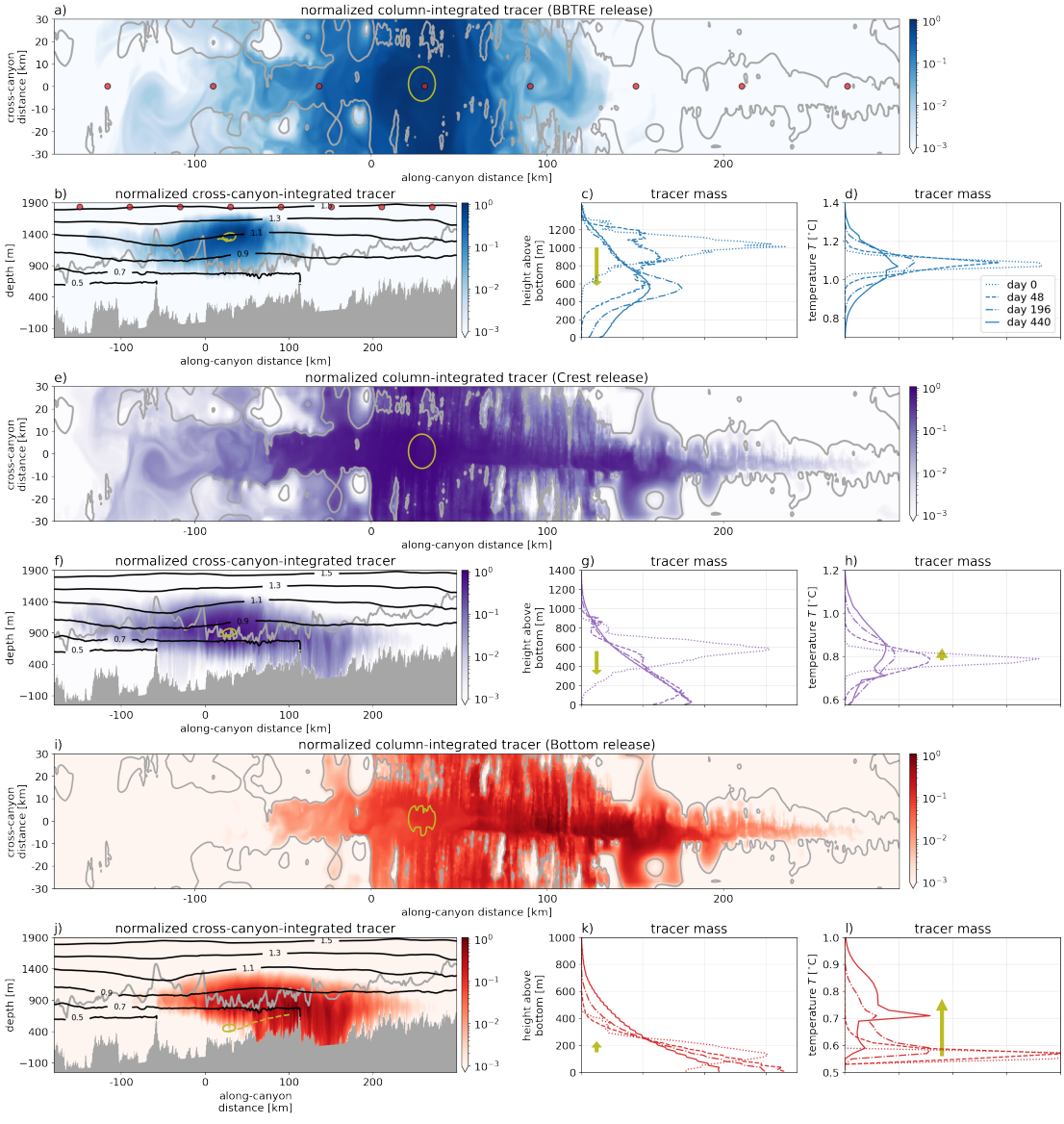

FIG. 5. Temporal evolution of the tracer distributions in Cartesian, height-above-bottom, and temperature coordinates for the BBTRE (a-d; blues), Crest (e-h; purples), and Bottom releases (i-l; reds). (a,e,i) Slope-normal column-integrated tracer concentrations and (b,f,j) cross-canyon-integrated tracer concentrations, shown 440 days after release and normalized by their instantaneous maximum value (logarithmic scale). Grey contours in (a,e,f) show two representative isobaths of ocean depth $\hat{d}(\hat{x},\hat{y})$. Black lines in (b,f,j) show equally-spaced cross-canyon-averaged temperature surfaces. Colored lines show normalized tracer distributions in (c,g,k) height-above-bottom and (d,h,l) temperature coordinates. Olive contours show the 10% contour for the initial tracer distributions; olive dashed lines and arrows show the temporal evolution of the tracer's center of mass (first moment) in the various coordinate frames from day 0 to 440. Red dots in (a,b) mark the locations used in the hypothetical sampling survey discussed in Section 4e.

Accepted for publication in *Journal of Physical Oceanography*. DOI 10.1175/JPO-D-22-0010.1.

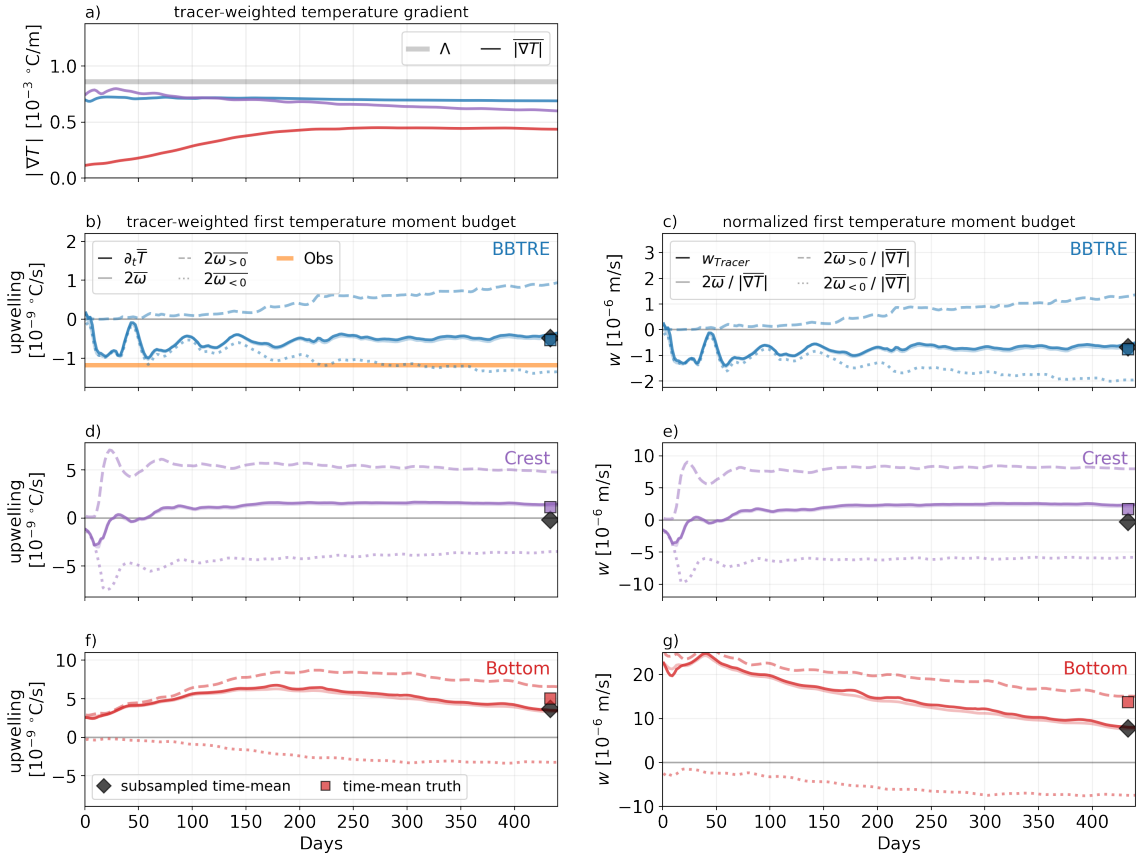

FIG. 6. First tracer-weighted temperature moment tendencies in temperature (left; eq. 3) and physical (right; eq. 5) space. The realistic BBTRE release is shown in blue, the Crest release in purple, and the Bottom release in red. (a) shows the temporal evolution of the tracer-weighted stratification, with the background stratification $\Lambda \equiv \frac{\mathrm{d}T_b}{\mathrm{d}\hat{z}}$ for reference (see Appendix A). (b-g) show the temporal evolution (opaque solid lines) of the first moment tendencies, which are visually indistinguishable from the mixing-driven buoyancy velocities that cause them (transparent solid lines; demonstrating that spurious numerical mixing is negligible). Dashed and dotted lines show the contributions from strictly upwelling and strictly downwelling regions, respectively. The orange line in (b) shows the time-averaged BBTRE moment tendencies estimated from observations (Ledwell et al. 1998, revised by Ledwell, in prep). Colored squares mark the time-mean, while the black diamonds mark the estimate of the time-mean from a realistically sparse sub-sampling of the simulated data (see Section 4e).

Accepted for publication in *Journal of Physical Oceanography*. DOI 10.1175/JPO-D-22-0010.1.

In the first 100 days, interpreting the mean diapycnal sinking of the BBTRE tracer is straightforward: the entire tracer distribution experiences a negative buoyancy velocity and so the tracer sinks diapycnally (Figure 6b), i.e. $\overline{\omega} \approx \overline{\omega_{<0}}$, where we define:

$$\overline{\omega_{<0}} \equiv \frac{\int_{\mathcal{V}_{\omega<0}} \omega\, c \,\mathrm{d}V}{\int_{\mathcal{V}} c \,\mathrm{d}V} \tag{12}$$

as the strictly-downwelling contribution to the tracer-averaged buoyancy velocity. While this strictly downwelling contribution strengthens slightly over the remainder of the experiment as the tracer sinks towards larger diffusivities, sufficient tracer is entrained into the BBL that a strictly upwelling contribution $\overline{\omega_{>0}}$ (similarly defined) grows at an even faster rate, such that the net diapycnal sinking of the tracer ($\overline{\omega} = \overline{\omega_{>0}} + \overline{\omega_{<0}}$) weakens over the remainder of the experiment (Figure 6b).

At the other extreme, the Bottom tracer is released entirely in the BBL and thus upwells vigorously across isopycnals upon release, with $\overline{\omega} \approx \overline{\omega_{>0}}$, and apparently accelerates over the first 200 days (Figure 6f). However, since the Bottom tracer is released near the bottom of a weakly stratified depression along the canyon thalweg, its average stratification increases dramatically over the first 200 days as it spreads to more stratified regions (Figure 6a); thus, when normalizing by a factor $|\nabla T|^{-1}$ to convert to physical space (eq. 5), the tracer-averaged upwelling rate instead decreases monotonically over time due to both an increasing tracer-averaged stratification and an increasing contribution from tracer that has spread into downwelling regions (Figure 6f,g).

The Crest release is perhaps the most interesting: at first, the Crest tracer is in the SML far above the canyon thalweg and thus downwells similarly to the BBTRE tracer; after roughly $\tau/2 = 23$ days, however, enough of the Crest tracer is advected into the BBLs along the rim of the canyon and the surrounding hills that the strictly upwelling component wins out and the tracer begins upwelling in the net (Figure 6d,e). Over the last few hundred days of the experiment, the weak net upwelling of the tracer is the small residual of a substantial compensation between strictly upwelling and strictly downwelling contributions.

By plotting the evolution of the tendency of the first temperature moment as a function of the tracer-weighted height-above-bottom (where $\eta \equiv z + d(x,y)$ is the height-above-bottom), we gain a qualitative sense of the height-above-bottom structure of the in-situ buoyancy velocity $\omega/|\nabla T|$ (Figure 7a). As the three tracers' centers of mass drift over time, their average buoyancy velocities

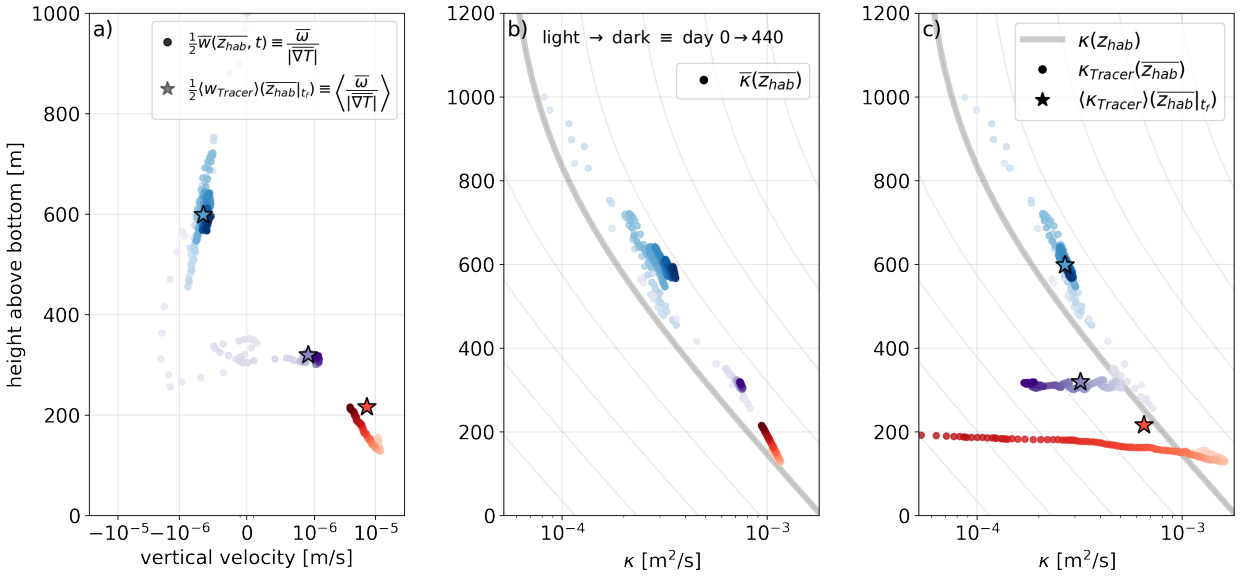

FIG. 7. (a) Tracer-weighted-average buoyancy velocities, normalized by the temperature gradient to yield an effective vertical velocity, as a function of tracer-weighted-average height-above-bottom $\overline{z_{\rm hab}}(t)$ (colors). The effective tracer diapycnal velocity is divided by 2 to yield an estimate of the in-situ diapycnal velocity $\omega/|\nabla T|$. (b,c) As in (a), but for the tracer-weighted in-situ diffusivity $\overline{\kappa}$ (eq. 14) and effective tracer diffusivity $\kappa_{\rm Tracer}$ (eq. 6). The colored dots (BBTRE in blue; Crest in purple; Bottom in red) darken over time, from 0 to 440 days. Stars in (a,c) show estimates of the time-averaged terms based on a single tracer survey at 440 days and knowledge of the release temperature (see Section 4e). The thick grey curves in (b,c) show the prescribed in-situ diffusivity profile; thin grey lines show the profile multiplied by factors of 2^n.

trace out a diapycnal downwelling that intensifies rapidly towards the bottom in the SML (Figure 7a, blue). Within about 300 m above the bottom, however, this downwelling gives way to upwelling (Figure 7a, purple) which intensifies the closer the tracer is to the bottom (Figure 7a, red).

Watermass transformations provide a helpful reference for contextualizing the magnitude and vertical structure of tracer-weighted velocities. In Appendix B, we convert the height-above-bottom (or η) structure of watermass transformations into an effective vertical velocity versus η-profile, $\overline{W}^T(\eta)$ (eq. B5; see Appendix B). This metric reveals that vigorous upwelling of $O(4\times10^{-5}\,\mathrm{m/s})$ is on average confined to the 40 m-thick BBL, largely compensated by downwelling that is an order of magnitude weaker—but also broader—in the SML above (Figure 8b-d, grey lines). Superficially, this seems to be inconsistent with the tracer diagnostics which exhibit weaker upwelling over a much thicker layer (8d, black dots).

Accepted for publication in *Journal of Physical Oceanography*. DOI 10.1175/JPO-D-22-0010.1.

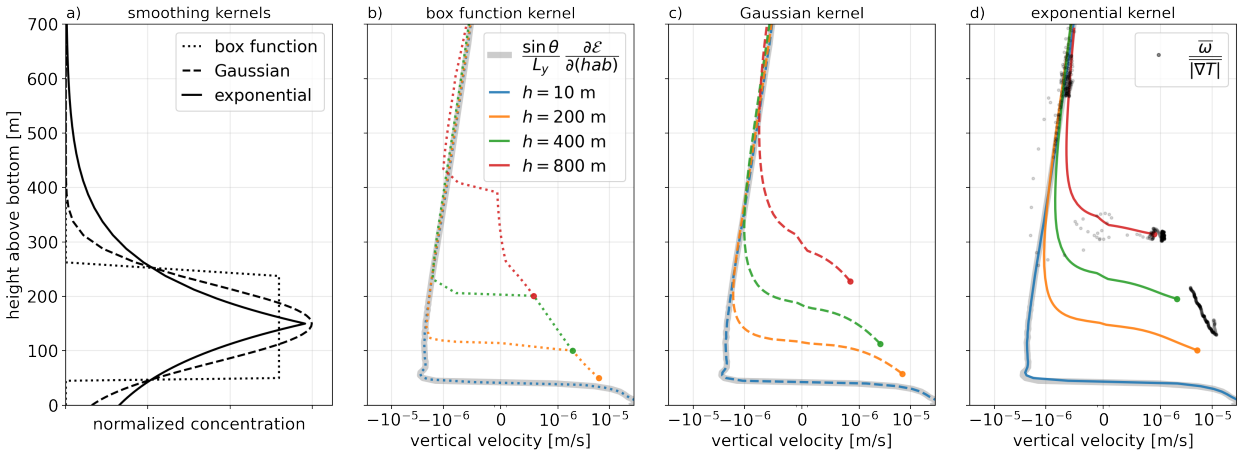

FIG. 8. Understanding the height-above-bottom structure of tracer transport by convolving the average velocity profile with idealized tracer kernels. (a) Three idealized shapes of tracer kernels, illustrated for a characteristic thickness of $h = 200$ m and centered at $\eta = 150$ m above the bottom. (b-d) Grey lines show the height-above-bottom averaged effective vertical velocity, estimated using watermass transformation analysis (eq. B5). Colored lines show the result of convolving this profile with idealized kernels (eq. 13) of different shapes (columns), widths (colors), and heights above bottom η' (y-axis). Black dots in (d) reproduce the snapshots of tracer-weighted buoyancy velocities shown in Figure 7a, for reference.

The key to reconciling the two diagnostics is that the tracer distributions, while initially compact, rapidly spread in η-space (Figure 5c,g,k). To demonstrate the effect of this spreading on the tracer diagnostics, we convolve the vertical velocity versus η-profile with smoothing tracer kernels of different shapes and widths (Figure 8a),

$$\overline{W}(\eta) \approx \int_{-\infty}^{\infty} \mathcal{K}(\eta - \eta')\overline{W}^T(\eta')\,\mathrm{d}\eta'. \tag{13}$$

Tracer kernels with widths less than the thickness of the BBL accurately reproduce the average η-structure of watermass transformations (8b-d, blue lines), while thicker kernels begin convolving the BBL upwelling and SML downwelling together, reducing their magnitudes and elevating the apparent interface between them (Figure 8b-d, other colors). This smearing effect of the convolution is particularly dramatic for exponential kernels with thick tails (Figure 8d, green and red lines), which reasonably approximates the shapes of the Crest and Bottom tracers for most of the experiment (Figure 5g,k). Indeed, convolving the vertical velocity η-profile with exponential

Accepted for publication in *Journal of Physical Oceanography*. DOI 10.1175/JPO-D-22-0010.1.

kernels of the same approximate width of these tracers roughly reproduces the tracer-diagnosed η-structure of the buoyancy velocity (Figure 8d). By contrast, the buoyancy velocity experienced by the BBTRE tracer is not as severely convolved (i.e. the dots near 600 m in Figure 8d fall on the grey curve of the in-situ buoyancy velocity) because the tracer remains sufficiently far above the bottom that it neither spreads as rapidly nor does it feel the compensating BBL upwelling (Figure 5c).

c. Bottom-enhanced diapycnal tracer spreading

Over the course of the experiment, all three tracers spread across isopycnals on average. As anticipated from the prescribed bottom-enhanced diffusivity profile: the closer a tracer is released to the bottom, the faster it spreads (Figure 7c; stars). However, this time-mean view obscures surprisingly large temporal variability (Figure 9). This tendency is particularly dramatic for the Bottom tracer, which experiences extremely rapid diapycnal spreading in the first 150 days but, by day 350, stops spreading entirely and even begins temporarily *contracting* in temperature space (Figure 9f,g)! The interpretation of diapycnal tracer spreading is more subtle than that of the mean diapycnal displacement of the tracer because two separate terms contribute to the spreading: the tracer-weighted effective diffusivity κ_{Taylor} and diapycnal distortion κ_ω (eq. 6). The contribution from the tracer-weighted effective diffusivity is familiar from Taylor (1922)'s classic derivation, and is reasonably well approximated by the tracer-weighted in-situ diffusivity $\overline{\kappa}$ since correlations between the diffusivity and the squared temperature gradients are relatively small (Figure 9c,e,g; compare dashed and dash-dotted lines),

$$\kappa_{\text{Taylor}} \equiv \frac{\overline{\kappa|\nabla T|^2}}{\overline{|\nabla T|^2}} \approx \overline{\kappa}, \tag{14}$$

i.e. squeeze dispersion only slightly modulates bulk tracer spreading (Wagner et al. 2019). This contribution to diapycnal spreading from the tracer-weighted diffusivity remains roughly constant in time, aside from an initial transient as the bulk of the tracer spreads towards shallower topographic features and therefore experiences more vigorous mixing on average (Figures 7b and 9c,e,g). The substantial temporal variability in the diapycnal spreading experienced by the tracers is instead driven by leading-order diapycnal distortion effects (Figure 9d-g). Depending on the instantaneous

distribution of the tracer in space, this term can vary substantially both in magnitude and sign, either amplifying the tracer-weighted diffusivity by up to 75% or neutralizing it entirely (Figure 9g; at 40 and 400 days, respectively).

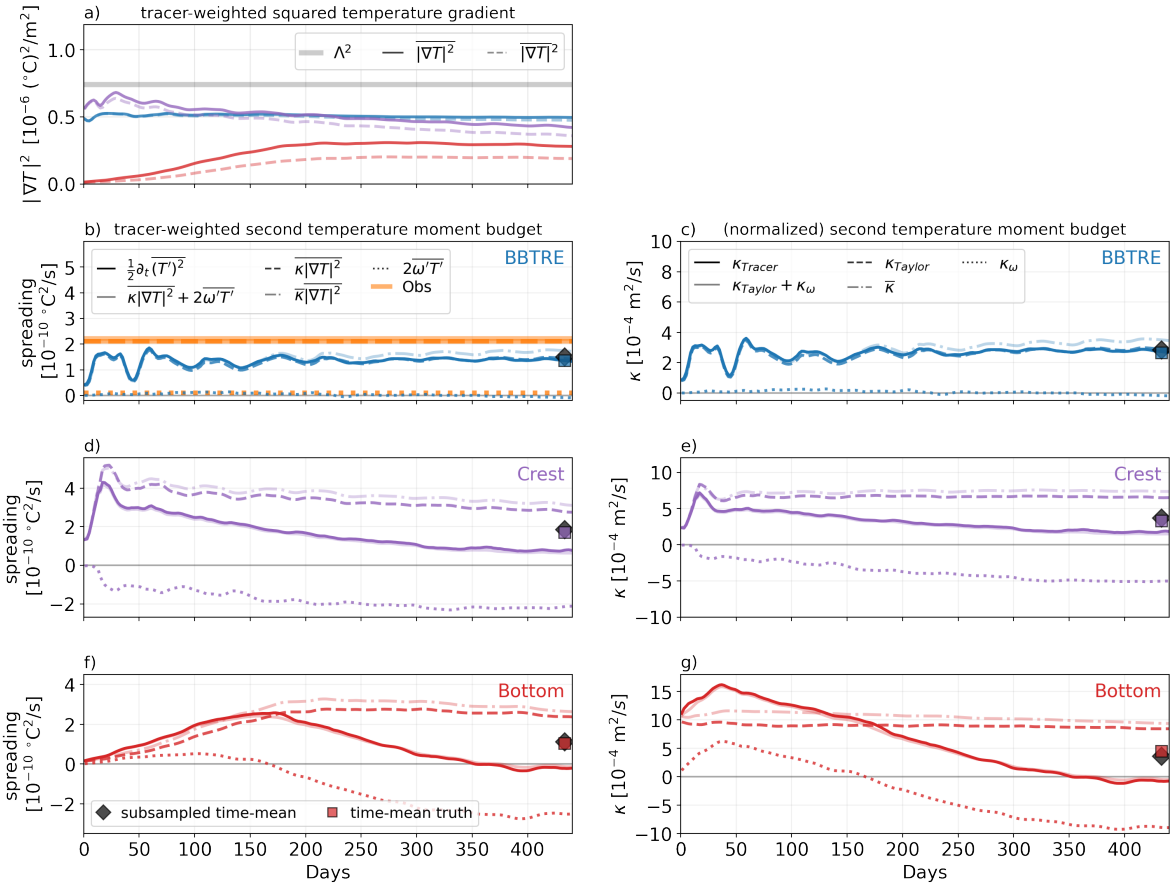

FIG. 9. As in Figure 6, but for the tracer-weighted centered second moment equations (4) and (6). Dash-dotted lines in (b-g) show the approximation of the diffusive term when correlations between κ and $|\nabla T|$ are ignored. Right-hand-side terms for the observations are estimated by applying the bottom-enhanced diffusivity profile that emerges from a 1D diffusion model (Ledwell, in prep); their sum is consistent with the left-hand-side measured from the diapycnal tracer spreading.

d. Untangling diapycnal distortion due to stretching and contraction effects

Motivated by the dipole example in Section 2b, we aim to gain a deeper understanding of these diapycnal distortion effects by decomposing the distortion term κ_ω in (ω, T) space (Figure 10, as

in Figure 1b), i.e. by decomposing the volume integral into a sum over sub-volumes:

$$\frac{\kappa_\omega}{\kappa_{\text{Taylor}}} = \sum_{i,j} \int_{\mathcal{V}_{\{\omega_i\}\cap\{T_j\}}} \frac{2\omega' T' c}{\mathcal{M}\,\overline{|\nabla T|^2}\,\kappa_{\text{Taylor}}}\,\mathrm{d}V, \tag{15}$$

where $\mathcal{M} \equiv \int_{\mathcal{V}} c\,\mathrm{d}V$ is the total tracer mass and the intersection of subsets $\{\omega_i\}$ and $\{T_j\}$ correspond to distinct sub-volumes $\mathcal{V}_{\{\omega_i\}\cap\{T_j\}}$ of the tracer distribution, defined by their (ω, T) characteristics. In (15) and throughout this section, we normalize by the total effective diapycnal diffusion κ_{Taylor} to quantify the relative importance of the unconventional distortion effects compared to the more conventional diapycnal (or vertical) diffusion (Taylor 1922); for example, $\kappa_\omega/\kappa_{\text{Taylor}} = 100\%$ implies stretching doubles the diffusive spreading rate while $\kappa_\omega/\kappa_{\text{Taylor}} = -100\%$ implies net contraction is sufficiently strong to exactly offset the diffusive contribution to spreading. Figure 10 shows heatmaps of the contributions from relatively narrow (ω', T') bins as well as the summed contributions from each of the quadrants delineated by the respective signs of ω' and T'. Figure 11 shows PDFs of tracer mass in (ω, T) space; by comparing with Figure 10, we attribute most of the diapycnal distortion to the small amounts of strongly anomalous tracer, i.e. with large $|\omega'|$ and $|T'|$.

We begin by exploring why the BBTRE tracer experiences very little net diapycnal distortion despite being stretched by strongly bottom-enhanced mixing (Ruan and Ferrari 2021). At day 100 (Figure 10a), we find the tracer is diapycnally stretched ($\overline{\omega' T'} > 0$) by an additional $23\%\kappa_{\text{Taylor}}$ (hereafter dropping the κ_{Taylor} for convenience) as relatively cold tracer relatively downwells ($T' < 0$, $\omega' < 0$; increasing spreading by 16%) and relatively warm tracer relatively upwells ($T' > 0$, $\omega' > 0$; increasing spreading by 7%). However, a very small amount of cold tracer has made it close enough to the seafloor to be entrained in the BBL, where it upwells sufficiently vigorously to result in a contraction effect of −9% which, supplemented by an additional −2% contraction from warm downwelling tracer, results in a reduction of the net diapycnal stretching to only $23\% - 11\% = 12\%$. By day 440 (Figure 10b), this cold patch of tracer is pulled further towards the bottom and its stretching effect grows to 69%, but is offset by an even larger diapycnal contraction of −76% in the BBL; combined with a net stretching of only $11\% - 10\% = 1\%$ from the warm tracer, diapycnal distortion has a negligible net contraction effect of −6%.

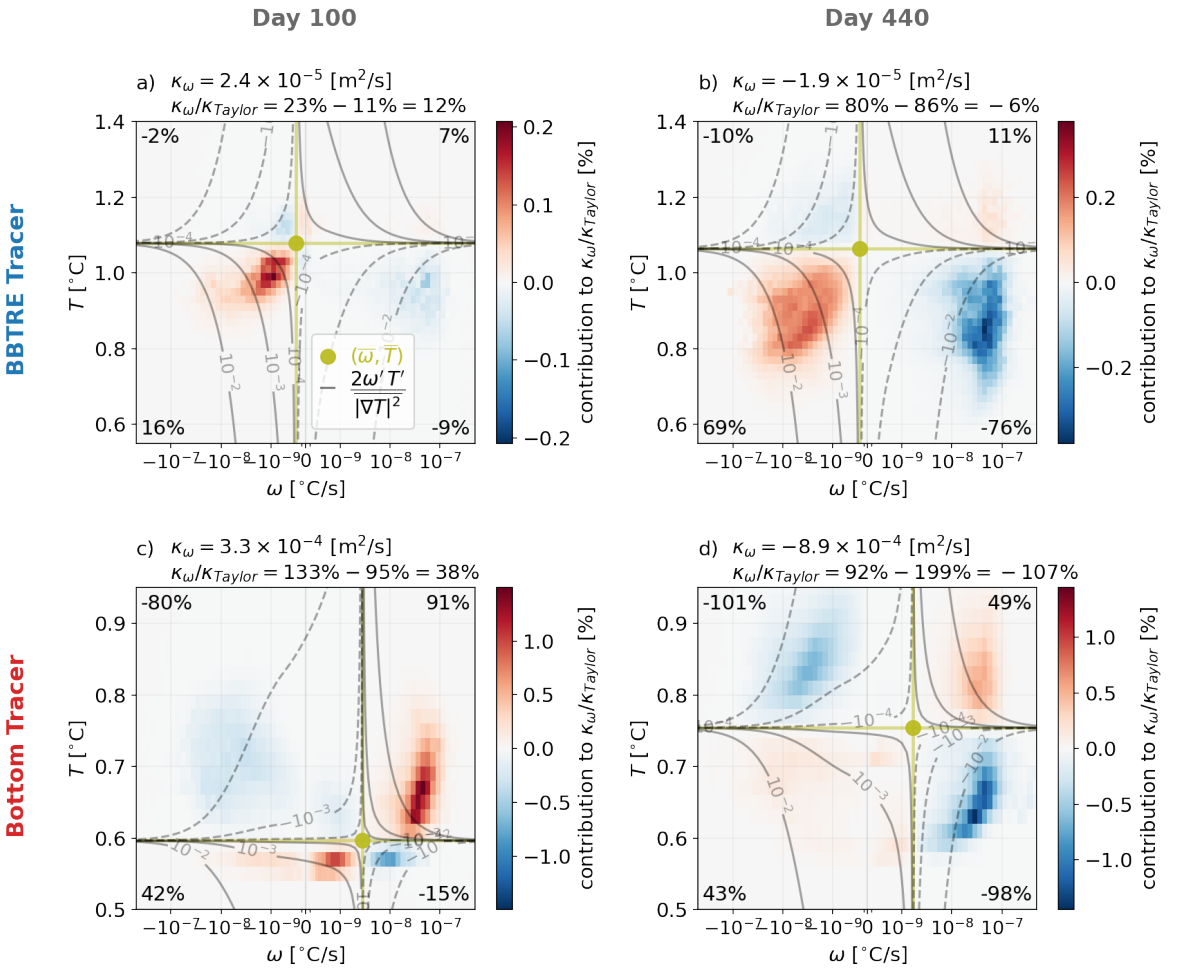

FIG. 10. Percentage contributions to the normalized net diapycnal distortion effect $\kappa_\omega/\kappa_{\text{Taylor}}$ from each (ω, T) bin, as a percentage, for the BBTRE (top) and Bottom (bottom) tracers at 100 days (left) and 440 days (right). The plotted quantity is the summand in eq. 15, which is integrated such that the contributions from each bin (log-spaced in ω) can be visually and quantitatively compared. Numbers in the four corners of each panel show the summed contributions from each of the four quadrants delineated by the respective signs of $\omega' \equiv \omega - \overline{\omega}$ and $T' \equiv T - \overline{T}$. The $\omega' = 0$ and $T' = 0$ lines in olive delineate the four quadrants. For reference, grey contours show the effective diapycnal distortion diffusivity, $\kappa_\omega \equiv 2\frac{\overline{\omega' T'}}{|\nabla T|^2}$, that corresponds to each (ω, T) bin. Sub-titles decompose the net diapycnal distortion effect into stretching ($\omega' T' > 0$) and contracting components ($\omega' T' < 0$).

At the other extreme, we aim to understand how the Bottom tracer undergoes first a large net diapycnal stretching effect and then an even larger net diapycnal contraction effect later on in its evolution. Over the first 100 days, most of the tracer upwells in the BBL and warms (Figure 6f).

Accepted for publication in *Journal of Physical Oceanography*. DOI 10.1175/JPO-D-22-0010.1.

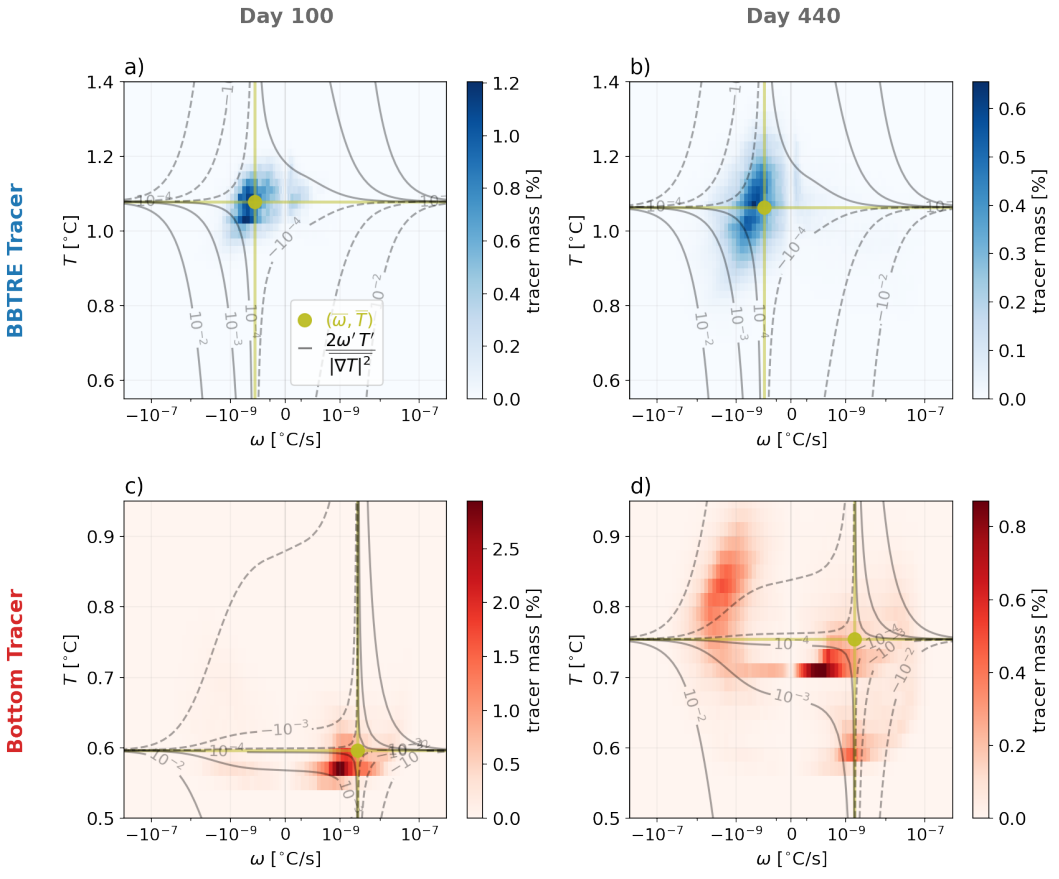

FIG. 11. Probability density function of tracer mass, as a percent contribution of each bin to the total tracer mass. Grey contours and olive lines as in Figure 10. The distributions seem skewed relative to the means because of the log-scale in ω.

Some of the warmest tracer remains in the BBL, where its upwelling drives a substantial diapycnal stretching of 91% (Figure 10c). However, part of this warm branch of the tracer is entrained into the SML, where its downwelling drives a largely compensating diapycnal contraction effect of −80%. The relatively cold patch of tracer that is left behind contributes a stretching of 42% − 15% = 27%, dominated by its relatively slow upwelling ($\omega > 0$ but $\omega' < 0$), bringing the net diapycnal stretching to 91% − 80% + 27% = 38%. By day 440, however, both the warm and cold branches of the tracer distribution (Figure 5l) drive large diapycnal contraction effects: −98% due to cold upwelling upstream of the sill and −101% due to warm downwelling downstream of the sill (Figures 5j,l and 10d). Diapycnal stretching of 93% from the other quadrants offset about half of this diapycnal

contraction, but the net diapycnal contraction of −106% still overwhelms the spreading due to the in-situ diffusivity, causing the Bottom tracer to temporarily contract in temperature space—contradicting conventional intuition about the bulk effects of down-gradient diapycnal diffusion!

e. Relevance to realistically sparse tracer surveys

The above results benefit from the luxury of knowing the exact tracer distributions $c(\mathbf{x},t)$ and temperature fields $T(\mathbf{x},t)$, as well as their instantaneous tendencies, everywhere and at all times; in practice, ship-board sampling strategies provide snapshots of c and T which are extremely sparse in both space and time.

Integrating the moment equations (3 and 4) between two surveys at t_i and $t_j = t_i + \Delta t$ yields more useful forms that at least do not depend on intractable time derivatives:

$$\frac{\overline{T}(t_j) - \overline{T}(t_i)}{\Delta t} = 2\langle\overline{\omega}\rangle \quad \text{and} \tag{16}$$

$$\frac{1}{2}\frac{\overline{(T')^2}(t_j) - \overline{(T')^2}(t_i)}{\Delta t} = \langle\overline{\kappa|\nabla T|^2} + 2\overline{\omega' T'}\rangle, \tag{17}$$

where $\langle\star\rangle \equiv \frac{1}{\Delta t}\int_{t_i}^{t_j} \star \, \mathrm{d}t$ denotes the time-mean. Tracers are typically injected along a chosen buoyancy surface, i.e. the initial conditions $\overline{T}(t_0) = T_0$ and $\overline{(T')^2}(t_0) \simeq 0$ are known *a priori* by design, allowing the moments to be estimated from a single survey at some time $t_j = t_0 + \Delta t$ after release. Figure 12 shows time-series of $\overline{T}(t)$ and $\overline{(T')^2}(t)$ for all three simulated tracer releases, from which the moments are readily calculated.

In practice, since the time between consecutive tracer surveys is typically much longer than their durations, a reasonable first approximation is to treat each observational survey as a snapshot in time, e.g. at the cruise's mid-point. Motivated by the BBTRE, in which the first major survey started roughly 14 months after release, we use (16) and (17) to *exactly* diagnose the time-mean moments (Figures 6b,d,f and 9b,d,f; colored squares) based only on a single instantaneous snapshot of the temperature and tracer fields 440 days (14.5 months) after release (Figure 12, colored squares).

Although temporal sparsity in sampling can be conveniently addressed in this way by integration, spatial sparsity requires a different approach. Motivated by the $O(60\,\mathrm{km})$ spacing of the BBTRE sampling strategy (Figure 2a; red dots), we generate synthetic tracer and buoyancy profiles by sub-sampling our simulation every 60 km along the thalweg of the canyon (Figure 5a,b; red dots).

One approach to making sense of this sparse data employs inverse methods, such as objective mapping, to estimate snapshots of the full three-dimensional tracer and buoyancy fields for each survey (as in Ledwell et al. 2000). Here, we take the much simpler approach of approximating the full three-dimensional tracer-weighted-volume-averages with tracer-weighted-sample-averages,

$$\frac{\int_{\mathcal{V}} c\phi \, \mathrm{d}V}{\int_{\mathcal{V}} c\phi \, \mathrm{d}V} \simeq \frac{\sum_{n,k} c(x_n, y_n, z_k)\phi(x_n, y_n, z_k)\Delta z(k)}{\sum_{n,k} c(x_n, y_n, z_k)\Delta z(k)}, \tag{18}$$

where subscript n and k denote the synthetic cast numbers and vertical levels, respectively, and $\Delta z(k)$ is the vertical resolution of the observations. This sample-averaging approach, which effectively ignores any horizontal covariance information, is similar in spirit to that used in many TRE analyses (e.g. Ledwell and Watson 1991; Ledwell et al. 1998; Holtermann et al. 2012; Watson et al. 2013). Despite this rather dramatic sub-sampling of our rich numerical solution, the tracer-weighted-sample-averaged estimates (18) generally yield estimates within 20% of the true time-mean (Figure 12; compare black diamonds to colored squares). The one exception is the Crest tracer's first-moment, for which the sample-averaged estimate suggests the tracer is slowly downwelling when it is in fact upwelling (Figure 12c); the Crest tracer's displacement is prone to large relative errors because it is the small residual of large upwelling and downwelling components.

By generating synthetic observations for all times between the tracer release and 440 days, we explore how the accuracy of the sampling strategy depends on the horizontal scales of the tracer distributions (Figure 12; grey lines). Estimates are likely to be error-prone until the initially narrow tracer distributions (with widths $\overline{(x')^2} = \sigma_x = 3.5\,\mathrm{km}$) have spread over horizontal distances comparable to the 60 km spacing of sampling stations. For example, estimates of the BBTRE moments are initially extremely noisy and only begin to stabilize when they reach a width of $\overline{(x')^2} \approx 20\,\mathrm{km}$ after about 200 days after release (Figure 12a,b). By contrast, the estimates for the Crest and Bottom release are much more stable (Figure 12c-f), presumably because the blocking of cross-canyon flow by the canyon sidewalls forces the tracer to homogenize more rapidly across the canyon, reducing the errors due to undersampling in the cross-canyon direction (see Figure 5). Interestingly, while the sample-averaged estimate of the Bottom tracer's spreading after 440

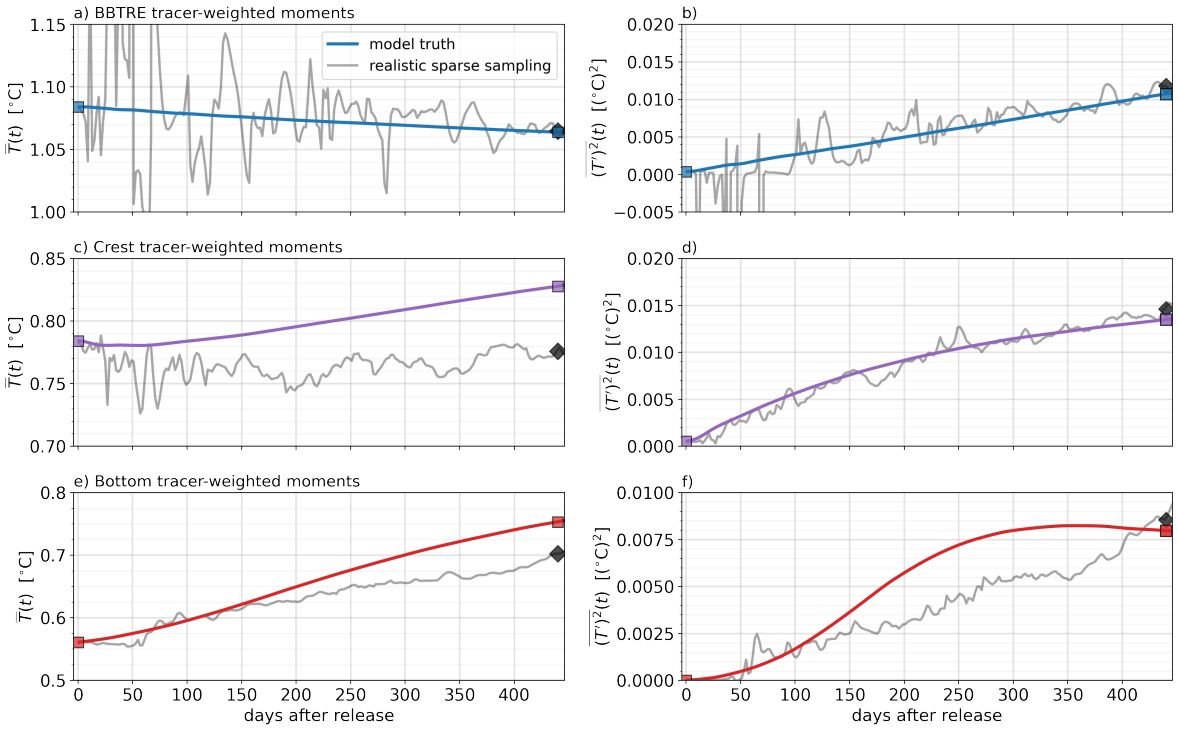

FIG. 12. Evolution of the first and (centered) second tracer-weighted temperature moments, exactly diagnosed from the full solution (colored lines) and estimated from a sparse sub-sampling (grey lines)—see sampling stations in Figure 5a,b. Squares denote the moments at days 0 and 440. Diamonds denote subsampled estimates of the moments at day 440, which can be combined with *a priori* knowledge of the tracer at day 0 to estimate equations (16) and (17).

days is reasonably accurate, earlier surveys would have completely missed the non-monotonic time-dependence caused by the leading-order diapycnal distortion effects (Figure 12f).

5. Discussion and Conclusion

By applying Ruan and Ferrari (2021)'s buoyancy moment diagnostics to our quasi-realistic regional simulation of mixing-driven abyssal flows (described in detail in a submitted companion manuscript, Drake et al. 2022), we confirm the qualitative results of Holmes et al. (2019)'s idealized analysis of the BBTRE release in the SML: over time, boundary suppression in the BBL almost exactly compensates for vertical stretching in the SML, such that the net diapycnal spreading of the BBTRE tracer coincidentally provides a reasonably accurate estimate (within 10%) of the tracer-weighted in-situ diffusivity (Figure 9c; compare black diamond with blue circle). These

simulation results are supported by a recent re-analysis of the BBTRE observations, which reveal a similarly negligible diapycnal distortion effect of $< 10\%\kappa_{\text{Taylor}}$ (Figure 9b; Ledwell, in prep).

Quantitatively, however, the diapycnal spreading we simulate for the BBTRE tracer is smaller than the observed spreading by roughly a factor of 2 (Figures 9c), suggesting either the microstructure measurements we use to tune the prescribed diffusivity profile are biased low or our simulation is missing other unknown tracer dispersion processes. This is roughly consistent with Ledwell's (in prep) inversion of a 1D advection-diffusion model, which produced optimal diffusivities about twice as large as the microstructure's sample-mean. Our results are also consistent with the conclusion of the submitted companion manuscript (Drake et al. 2022), which shows that biases in the simulated flows and stratification of the BBTRE fracture zone canyon also suggest the imposed microstructure mixing rates may be biased low by a factor of roughly 2. These BBTRE-specific results are consistent with the broader observational literature, which unanimously finds that mixing rates estimated from TREs are larger than those suggested by co-located microstructure measurements (Ruan and Ferrari 2021).

In contrast to the BBTRE release, we find that for near-bottom tracers, diapycnal distortion can be of either sign (depending on the tracer distribution) and of comparable magnitude to the tracer-weighted in-situ diffusivity, $|\kappa_\omega| \sim \kappa_{\text{Taylor}} \simeq \overline{\kappa}$ (Figure 9g). Our simulations demonstrate that three-dimensional eddies and topographic effects have a leading order impact on diapycnal tracer spreading, as tracer distributions are chaotically transported in and out of regions of vigorous mixing. Unsurprisingly, diapycnal stretching and contraction effects are much stronger—and more variable—in our three dimensional flows over rough topography than the already substantial effects reported by Holmes et al. (2019) for one-dimensional boundary layers with parameterized isopycnal eddy stirring. In all of Holmes et al.'s (2019) near-bottom releases, diapycnal contraction reduces spreading rates by a factor of 2–3, which even in the case of vigorous isopycnal stirring only slightly deviates from predicted factor of $\left(1 - \frac{2}{\pi}\right)^{-1} \approx 2.8$ for the long-time limit of 1D diffusion on the half-line. By contrast, for our Bottom tracer release, diapycnal distortion amplifies diapycnal spreading by a stretching of $O(75\%\kappa_{\text{Taylor}})$ in the first few dozen days of the simulation and later suppresses diapycnal spreading by a contraction of $O(-100\%\kappa_{\text{Taylor}})$ for the last few dozen days (Figures 9g; 7c)!

Given that rough topography generally implies strong bottom-enhanced diapycnal mixing (Polzin et al. 1997; Waterhouse et al. 2014), which is in turn thought to incite bottom mixed layer eddies (Callies 2018; Wenegrat et al. 2018; Ruan and Callies 2020), significant diapycnal stretching and contraction effects are to be expected near sloping rough topography in the abyss, such as along the global mid-ocean ridge system (Ledwell et al. 2000; Thurnherr et al. 2005, 2020) and within continental slope canyons (Nazarian et al. 2021; Hamann et al. 2021; Alberty et al. 2017). In these regions, unlike for interior ocean releases such as BBTRE, tracer-based estimates of mixing rates must take into account the three-dimensional history of the tracer distribution's evolution.

It has long been appreciated that the interpretation of tracer spreading near topography requires greater care because of enhanced boundary mixing and hypsometric effects (e.g. Ledwell and Hickey 1995). Attempts to modify the conventional 1D model to include these boundary effects are varied: e.g., by separately modeling the tracer distribution in "boundary" and "interior" regions (Ledwell and Hickey 1995; Holtermann et al. 2012; Ledwell et al. 2016), by allowing vertical structure in the diffusivity and hypsometry in 1D advection-diffusion models (Ledwell et al. 2000; Holtermann et al. 2012), or by extending the 1D model to a 2D (Watson et al. 2013) or 3D (Mackay et al. 2018) model to account for lateral transport into and out of regions of strong mixing. However, the *ad hoc* derivations of these models render them difficult to interpret and compare, suggesting a complementary role for the more exact buoyancy moment approach (Holmes et al. 2019; Ruan and Ferrari 2021).

Mesoscale/submesoscale-resolving regional simulations of TREs are now feasible thanks to exponential increases in computational power (Tulloch et al. 2014; Mashayek et al. 2017; Ogden et al., in prep; this study) and have been used *a posteriori* to help interpret observations and explain differences between mixing rates inferred from TREs and microstructure profiles. However, such simulations have not yet been used to evaluate (or improve upon) operational methods for comparing tracer and microstructure observations, such as by using a "perfect model" framework in which simulated tracer observations are inverted in an attempt to recover the prescribed "true" diffusivity field. As an illustrative example, in Section 4e, we attempt to estimate in-situ diffusivities by applying the exact buoyancy moment approach to realistically-sparse synthetic observational campaigns. The results suggest that diapycnal distortion effects, which are poorly represented within conventional inverse models, result in $O(1)$ structural errors in estimates of the tracer-

weighted in-situ diffusivity $\overline{\kappa}$. Sampling errors are relatively small ($< 20\%$) by comparison and are likely overestimated here because our BBTRE simulation underestimates the observed isopycnal spreading rate (and thus the effective horizontal sampling resolution) by roughly a factor of five (Ledwell et al. 2000) due to the exclusion of externally-forced currents and mesoscale stirring in our narrow simulation domain.

In the future, *a priori* or real-time numerical simulations could be used to inform TRE sampling strategies—current best practice is to roughly estimate horizontal transport from real-time velocity estimates from ADCPs or altimetry (Messias and Ledwell, personal communication). To our knowledge, this has not yet been done, with the notable exception of the *Bottom Boundary Layer Turbulence and Abyssal Recipes* team (BLT; NSF Award #1756251), who are using TRE simulations to inform the experiment's planning and sampling strategies.

While our results suggest that estimates of in-situ diffusivity profiles from observations of a tracer's *second* buoyancy moment may be corrupted by complicated diapycnal distortion processes (Figure 7c; consistent with Holmes et al. 2019), they also support Holmes et al. (2019)'s hypothesis that the *first* buoyancy moment provides a more robust and straight-forward estimate of the in-situ turbulent buoyancy flux convergence (or buoyancy velocity ω; Figure 7a). However, even the first moment diagnostics can be misleading convolutions of opposing upwelling and downwelling components (Figure 8), making them challenging to interpret and prone to significant sampling errors (Figure 12c). Nevertheless, as long as a sizable fraction (here $\gg \overline{W}^T_{\mathrm{SML}}/\overline{W}^T_{\mathrm{BBL}} \approx 10\%$; Figure 8) of the tracer remains in the BBL and the sampling resolution is sufficiently high, the change in the first buoyancy moment is likely to provide at least a reasonable lower-bound estimate of the average in-situ upwelling in the BBL (Section 2b). This is a promising result in light of the ongoing BLT TRE, which aims to provide the first in-situ estimates of BBL upwelling. Short-term surveys, when the tracer distribution is still relatively compact (e.g. from a dye release experiment), may be interpreted as lower bound estimates of BBL upwelling; on the other hand, long-term surveys, when the tracer roughly equally occupies the BBL and SML, may be interpreted as estimates of net upwelling. Combined, these two estimates could constrain the strength of the amplification factor (the ratio of strictly upwelling transport in the BBL to net upwelling), which is predicted by theory to be much larger than 1 but remains poorly understood (Ferrari et al. 2016; McDougall and Ferrari 2017; Callies 2018; Holmes and McDougall 2020). In combination with previous observations

of tracer-weighted diapycnal sinking in the SML above rough topography (Ledwell et al. 2000), observations of vigorous tracer-weighted diapycnal upwelling in the BBL would be compelling direct evidence for the emerging paradigm of bottom mixing layer control of the abyssal meridional overturning circulation (Ferrari et al. 2016; de Lavergne et al. 2016a; Callies 2018; Callies and Ferrari 2018; Drake et al. 2020; submitted companion manuscript, Drake et al. 2022).

Acknowledgments. We thank Jim Ledwell for countless insightful discussions about this work and comments on previous versions of the manuscript. We also thank Ryan Holmes and an anonymous reviewer for suggestions that improved the manuscript. We thank the crews of the BBTRE and DoMORE field campaigns for collecting the observations that motivated this work. We acknowledge funding support from National Science Foundation Awards 1536515 and 1736109. This material is based upon work supported by the National Science Foundation Graduate Research Fellowship Program under Grant No. 174530. Any opinions, findings, and conclusions or recommendations expressed in this material are those of the author(s) and do not necessarily reflect the views of the National Science Foundation. This research is also supported by the NOAA Climate and Global Change Postdoctoral Fellowship Program, administered by UCAR's Cooperative Programs for the Advancement of Earth System Science (CPAESS) under award #NA18NWS4620043B.

Data availability statement. The source code for the MITgcm simulations and all of the Python code necessary to produce the figures will be publicly available at `github.com/hdrake/sim-bbtre` upon acceptance (or earlier by requesting the corresponding author). Our analysis of labeled data arrays is greatly simplified by the `xarray` package in Python (Hoyer and Hamman 2017).

APPENDIX A

A slope-native MITgcm configuration of bottom mixing layer flows in the Brazil Basin

We use a hydrostatic formulation of the MIT General Circulation Model (MITgcm; Marshall et al. 1997) to simulate mixing-driven flows in the BBTRE canyon and the transient evolution of three localized tracer releases. Regional bathymetry is extracted from the Global Bathymetry and Topography at 15 Arc Sec dataset (SRTM15+; Tozer et al. 2019) and interpolated onto a locally-tangent Cartesian grid $(\hat{x}, \hat{y}, \hat{z})$ aligned with the BBTRE canyon, where $\hat{x}$ denotes the along-canyon (or cross-ridge) dimension, $\hat{y}$ denotes the cross-canyon (or along-ridge) dimension, and $\hat{d}(\hat{x}, \hat{y})$ is the seafloor depth (Figure 2a). The domain includes both the BBTRE tracer release location and ample room for up-canyon advection of the tracer, which is anticipated based on both the BBTRE observations (Ledwell et al. 2000) and bottom boundary layer theory (Holmes et al. 2019).

Inspired by 1D boundary layer theory and the idealized 3D simulations of Callies (2018), we configure a slope-native implementation of the MITgcm (only summarized here; details in Drake et al. 2022). First, we separate a quiescent ($\mathbf{u}_b \equiv \mathbf{0}$) background with uniform stratification $\Lambda \equiv \frac{\mathrm{d}T_b}{\mathrm{d}\hat{z}} = 9\times10^{-4}\,^\circ\mathrm{C/m}$ from the solution and solve only for the perturbations $T_p \equiv T - T_b$ and $\mathbf{u}_p \equiv \mathbf{u}$ about this background state, which requires adding the appropriate tendency terms to the perturbation temperature and momentum equations, respectively. Second, we transform the MITgcm into the coordinates of the mean slope, with slope angle $\theta = 1.26\times10^{-3}$ (Figure 2b), allowing us to apply periodic boundary conditions to the perturbations T_p and $\mathbf{u}_p$ (and the released tracer concentration c) in the (x, y) plane of the mean slope. The de-trended seafloor depth is given by $d(x, y) \equiv \hat{d}(\hat{x}, \hat{y}) - \hat{x}\tan\theta$. Mean cross-slope (along-canyon) upwelling and downwelling across the periodic $\mathbf{x}$ boundary provide infinite sources of dense and light waters, respectively, allowing equilibration of the solution without requiring an explicit restoring force to balance the homogenizing tendency of turbulent mixing (Garrett 1991).

A companion paper (Drake et al. 2022) explores the mixing-driven circulations that arise in this simulation in detail. Bottom-enhanced mixing spins up a broad diapycnal sinking in the well-stratified interior and a vigorous diabatic upwelling in the bottom boundary layer. Despite a modest restratifying effect by this mean overturning circulation, the solution develops a substantial horizontal temperature gradient which stores available potential energy. This available potential energy fuels instabilities, which grow to finite amplitude and are characterized by a Rossby number of $R_o \approx 1$, i.e. are submesoscale in nature (see e.g. McWilliams 2016). One effect of these eddies is to restratify the bottom 20 m or so, bringing the simulated stratification more in line with observations than 1D boundary layer dynamics would suggest (Callies 2018; Ruan and Callies 2020). A hierarchy of progressively simplified versions of the simulation are used as mechanism denial experiments to show the importance of topographic blocking and steering in controlling the near-bottom stratification, which in turn controls the magnitude of near-bottom diapycnal upwelling.

In our slope-native configuration, one should imagine infinitely many copies of the TRE, each separated by a horizontal distance $L_x = 480\,\mathrm{km}$ (domain length) and vertical height $L_x\tan\theta \approx 1000\,\mathrm{m}$ (corresponding to a background temperature difference $\Delta T \approx \frac{\mathrm{d}T_b}{\mathrm{d}\hat{z}} L_x \sin\theta = 0.52\,^\circ\mathrm{C}$). A limitation of this configuration is that when tracer crosses the $\mathbf{x}$-boundary, it experiences an

unphysical jump in temperature of ΔT. This problem can be significantly delayed, but not avoided entirely, by re-centering the domain around the tracer blobs before adding the constantly-stratified background temperature field T_b back in (e.g., see Figure 5). By 1000 days, however, enough of the tracer has crossed the periodic **x**-boundaries that the copies of the tracers begin significantly interfering with each other and the temperature moment calculations become meaningless. This does not affect the results presented here since we truncate the simulations after the timing of the first BBTRE survey (14 months ≈ 440 days), well before these issues arise. For all of the analysis presented here, we crop the infinitely-repeating domain to include only a single copy of the tracer distribution (similar to the approach used to compute watermass transformations in Appendix B).

APPENDIX B

Eulerian and tracer-weighted watermass transformations

A natural framework for understanding the drivers of diapycnal transport is watermass transformation analysis (Walin 1982; Marshall et al. 1999), which reframes the buoyancy budget in buoyancy space by integrating along buoyancy surfaces (or over buoyancy classes). Following Ferrari et al. (2016), the diapycnal transport $\mathcal{E}(T,t)$ across a buoyancy surface $\mathcal{A}(T)$ is given by

$$\mathcal{E}(T,t) \equiv \iint_{\mathcal{A}(T)} \mathbf{e}\cdot\mathbf{n}\,\mathrm{d}A = \partial_T \int_{\mathcal{V}(\tilde{T}<T)} \omega\,\mathrm{d}V, \tag{B1}$$

where $\mathbf{e} \equiv \left(\mathbf{u}\cdot\mathbf{n} - \frac{T_t}{|\nabla T|}\right)\mathbf{n}$ is the diapycnal velocity and $\mathcal{V}(\tilde{T}<T)$ is the volume enclosing any water denser than T. Since our simulations have not fully equilibrated in the SML, diapycnal transports include two components: flow across a buoyancy surface and the movement of the buoyancy surfaces themselves. In the present context, it is useful to distinguish contributions to the diapycnal transport from a strictly upwelling BBL component, where the integral is only evaluated over the strictly upwelling volume $\mathcal{V}(\tilde{T}<T;\omega>0)$, and a strictly downwelling SML component, similarly defined (see Figure B1).

In practice, meaningful evaluation of this integral in the slope-native configuration requires stitching together $H/(L_x\tan\theta) \approx O(5)$ periodic copies of the domain (where H is the height of the domain) before adding in the background buoyancy field B, so that each isopycnal can be followed all the way from where it intersects with the seafloor to the interior far-field where mixing

is weak (Figure B1). Further, because our simulation is periodic in the cross-slope (along-canyon) direction **x** (and thus in mean buoyancy), the resulting watermass transformations are periodic over a buoyancy interval $\Delta T = \Lambda L_x \tan\theta \approx 0.52\,^\circ\mathrm{C}$. Temporal variability of watermass transformations is small relative to the other variations we focus on, so all results hereafter refer to their time-mean.

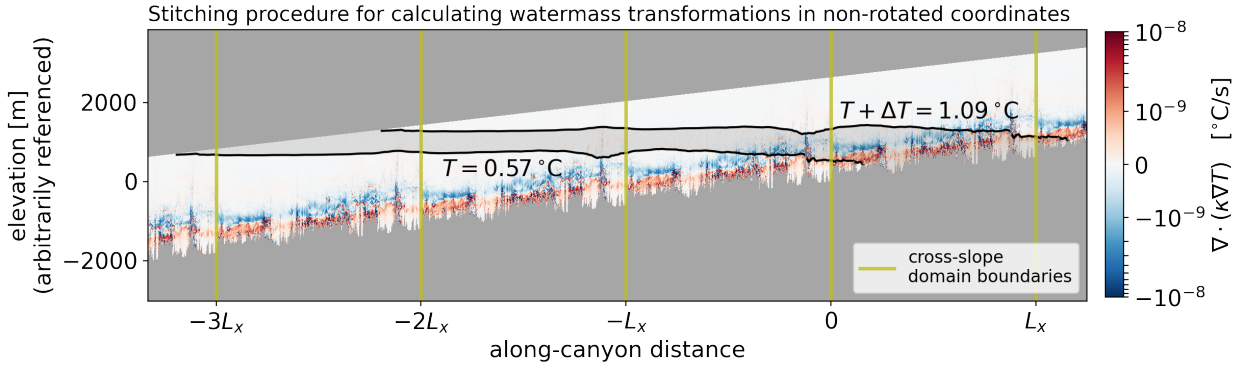

FIG. B1. Turbulent buoyancy (temperature) flux convergence along the trough of the BBTRE canyon. Vertical olive lines show along-canyon boundaries of the simulation domain; the solution is doubly periodic in buoyancy perturbations, but discontinuous in the total buoyancy in the along-canyon direction due to a constant background mean slope and stratification. For the small mean slopes considered here, computing watermass transformations thus requires reconstructing the full extent of buoyancy surfaces by stitching together multiple copies of the domain, each translated by a multiple of the domain extent L_x and by a background temperature jump $\Delta T = \Lambda\,\Delta z \approx 0.52\,^\circ\mathrm{C}$ (where $\Delta z = L_x \tan\theta$ is the layer thickness).

Averaging over a buoyancy layer of thickness ΔT yields a single representative value of the net watermass transformation,

$$\overline{\mathcal{E}}^{T} \equiv \frac{1}{\Delta T}\int_{T}^{T+\Delta T} \mathcal{E}(\tilde{T})\,\mathrm{d}\tilde{T} = \int_{\mathcal{V}(T<\tilde{T}<T+\Delta T)} \frac{\omega}{\Delta T}\,\mathrm{d}V. \tag{B2}$$

This equation is also reminiscent of that for the evolution of the first tracer-weighted buoyancy moment (5), with the whole domain being weighted equally as opposed to being weighted by the tracer concentration.

The detailed height-above-bottom (η, for short) structure of upwelling and downwelling watermass transformations are also of interest, since these are more directly comparable with measurements from vertical profilers, 1D BBL theory, and the diapycnal transport of localized tracers. Building upon Holmes and McDougall (2020), we define the height-above-bottom cumulative

watermass transformation as:

$$\overline{\mathcal{E}}^{T}(\eta) = \int_{\mathcal{V}(T_0<\tilde{T}<T_0+\Delta T;\, \tilde{\eta}<\eta)} \frac{\omega}{\Delta T}\, \mathrm{d}V. \tag{B3}$$

We aim to convert these watermass transformations into effective vertical velocities, for more direct comparison with the tracer diagnostics. Loosely, taking the slope-normal (or η) derivative provides the up-slope upwelling flux (in m^2/s) at a given height-above-bottom:

$$\frac{\partial}{\partial \eta}\overline{\mathcal{E}}^{T}(\eta) = \frac{\partial}{\partial \eta}\int_{\mathcal{V}(T_0<\tilde{T}<T_0+\Delta T;\, \tilde{\eta}<\eta)} \frac{\omega}{\Delta T}\, \mathrm{d}V. \tag{B4}$$

Multiplying by $\sin\theta$ approximately converts this to a vertical flux, and dividing by the width L_y of the domain finishes the conversion to the effective velocity (B5),

$$\overline{W}^{T}(\eta) \equiv \frac{\sin\theta}{L_y}\, \frac{\partial}{\partial \eta}\overline{\mathcal{E}}^{T}(\eta). \tag{B5}$$

Profiles of $\overline{W}^{T}(\eta)$ are shown in Figure 8 and, after convolution with idealized height-above-bottom tracer distributions, compare favorably with the diagnosed vertical structure of tracer upwelling.

References

Abernathey, R. P., I. Cerovecki, P. R. Holland, E. Newsom, M. Mazloff, and L. D. Talley, 2016: Water-mass transformation by sea ice in the upper branch of the Southern Ocean overturning. *Nature Geoscience*, **9 (8)**, 596–601, https://doi.org/10.1038/ngeo2749, URL http://www.nature.com/articles/ngeo2749, publisher: Nature Publishing Group.

Alberty, M. S., S. Billheimer, M. M. Hamann, C. Y. Ou, V. Tamsitt, A. J. Lucas, and M. H. Alford, 2017: A reflecting, steepening, and breaking internal tide in a submarine canyon. *Journal of Geophysical Research: Oceans*, **122 (8)**, 6872–6882, https://doi.org/10.1002/2016JC012583, URL https://onlinelibrary.wiley.com/doi/abs/10.1002/2016JC012583, _eprint: https://onlinelibrary.wiley.com/doi/pdf/10.1002/2016JC012583.

Baker, M. A., and C. H. Gibson, 1987: Sampling Turbulence in the Stratified Ocean: Statistical Consequences of Strong Intermittency. *Journal of Physical Oceanography*,

17 (10), 1817–1836, https://doi.org/10.1175/1520-0485(1987)017<1817:STITSO>2.0.CO;2, URL https://journals.ametsoc.org/view/journals/phoc/17/10/1520-0485_1987_017_1817_stitso_2_0_co_2.xml, publisher: American Meteorological Society Section: Journal of Physical Oceanography.

Bryan, K., and L. J. Lewis, 1979: A water mass model of the world ocean. *Journal of Geophysical Research*, **84 (C5)**, 2503–2517, https://doi.org/10.1029/JC084iC05p02503, iSBN: 0148-0227.

Cael, B., and A. Mashayek, 2021: Log-Skew-Normality of Ocean Turbulence. *Physical Review Letters*, **126 (22)**, 224 502, https://doi.org/10.1103/PhysRevLett.126.224502, URL https://link.aps.org/doi/10.1103/PhysRevLett.126.224502, publisher: American Physical Society.

Callies, J., 2018: Restratification of Abyssal Mixing Layers by Submesoscale Baroclinic Eddies. *Journal of Physical Oceanography*, JPO–D–18–0082.1, https://doi.org/10.1175/JPO-D-18-0082.1, URL http://journals.ametsoc.org/doi/10.1175/JPO-D-18-0082.1.

Callies, J., and R. Ferrari, 2018: Dynamics of an Abyssal Circulation Driven by Bottom-Intensified Mixing on Slopes. *Journal of Physical Oceanography*, **48 (6)**, 1257–1282, https://doi.org/10.1175/JPO-D-17-0125.1, URL http://journals.ametsoc.org/doi/10.1175/JPO-D-17-0125.1.

Clément, L., A. M. Thurnherr, and L. C. St. Laurent, 2017: Turbulent Mixing in a Deep Fracture Zone on the Mid-Atlantic Ridge. *Journal of Physical Oceanography*, **47 (8)**, 1873–1896, https://doi.org/10.1175/JPO-D-16-0264.1, URL http://journals.ametsoc.org/doi/10.1175/JPO-D-16-0264.1.

de Lavergne, C., G. Madec, J. Le Sommer, A. J. G. Nurser, and A. C. Naveira Garabato, 2016a: The Impact of a Variable Mixing Efficiency on the Abyssal Overturning. *Journal of Physical Oceanography*, **46 (2)**, 663–681, https://doi.org/10.1175/JPO-D-14-0259.1, URL http://journals.ametsoc.org/doi/10.1175/JPO-D-14-0259.1.

de Lavergne, C., G. Madec, J. Le Sommer, A. J. G. Nurser, and A. C. Naveira Garabato, 2016b: On the Consumption of Antarctic Bottom Water in the Abyssal Ocean. *Journal of Physical Oceanography*, **46 (2)**, 635–661, https://doi.org/10.1175/JPO-D-14-0201.1, URL http://journals.ametsoc.org/doi/10.1175/JPO-D-14-0201.1.

de Lavergne, C., and Coauthors, 2020: A Parameterization of Local and Remote Tidal Mixing. *Journal of Advances in Modeling Earth Systems*, **12 (5)**, e2020MS002 065, https://doi.org/https://doi.org/10.1029/2020MS002065, URL https://agupubs.onlinelibrary.wiley.com/doi/abs/10.1029/2020MS002065, _eprint: https://agupubs.onlinelibrary.wiley.com/doi/pdf/10.1029/2020MS002065.

De Szoeke, R. A., and A. F. Bennett, 1993: Microstructure Fluxes across Density Surfaces. *Journal of Physical Oceanography*, **23 (10)**, 2254–2264, https://doi.org/10.1175/1520-0485(1993)023<2254:MFADS>2.0.CO;2, URL https://journals.ametsoc.org/doi/abs/10.1175/1520-0485(1993)023%3C2254:MFADS%3E2.0.CO%3B2, publisher: American Meteorological Society.

Dematteis, G., and Y. V. Lvov, 2021: Downscale energy fluxes in scale-invariant oceanic internal wave turbulence. *Journal of Fluid Mechanics*, **915**, https://doi.org/10.1017/jfm.2021.99, URL https://www.cambridge.org/core/journals/journal-of-fluid-mechanics/article/downscale-energy-fluxes-in-scaleinvariant-oceanic-internal-wave-turbulence/575CD634A844D7DACF84EBBA9FF5A084, publisher: Cambridge University Press.

Dillon, T. M., 1982: Vertical overturns: A comparison of Thorpe and Ozmidov length scales. *Journal of Geophysical Research: Oceans*, **87 (C12)**, 9601–9613, https://doi.org/https://doi.org/10.1029/JC087iC12p09601, URL https://agupubs.onlinelibrary.wiley.com/doi/abs/10.1029/JC087iC12p09601, _eprint: https://agupubs.onlinelibrary.wiley.com/doi/pdf/10.1029/JC087iC12p09601.

Drake, H. F., 2021: Control of the abyssal ocean overturning circulation by mixing-driven bottom boundary layers. Thesis, Massachusetts Institute of Technology and Woods Hole Oceanographic Institution, https://doi.org/10.1575/1912/27424, URL https://darchive.mblwhoilibrary.org/handle/1912/27424, accepted: 2021-08-10T15:07:15Z.

Drake, H. F., R. Ferrari, and J. Callies, 2020: Abyssal Circulation Driven by Near-Boundary Mixing: Water Mass Transformations and Interior Stratification. *Journal of Physical Oceanography*, **50 (8)**, 2203–2226, https://doi.org/10.1175/JPO-D-19-0313.1, URL https://journals.ametsoc.org/jpo/article/50/8/2203/348530/

Abyssal-Circulation-Driven-by-Near-Boundary-Mixing, publisher: American Meteorological Society.

Drake, H. F., X. Ruan, R. Ferrari, A. M. Thurnherr, K. Ogden, and J. Callies, 2022: Dynamics of eddying abyssal mixing layers over rough topography. URL https://eartharxiv.org/repository/view/3000/, publisher: EarthArXiv.

Ferrari, R., A. Mashayek, T. J. McDougall, M. Nikurashin, and J.-M. Campin, 2016: Turning Ocean Mixing Upside Down. *Journal of Physical Oceanography*, **46 (7)**, 2239–2261, https://doi.org/10.1175/JPO-D-15-0244.1, URL http://journals.ametsoc.org/doi/10.1175/JPO-D-15-0244.1.

Garrett, C., 1991: Marginal mixing theories. *Atmosphere-Ocean*, **29 (2)**, 313–339, https://doi.org/10.1080/07055900.1991.9649407, URL https://doi.org/10.1080/07055900.1991.9649407, publisher: Taylor & Francis _eprint: https://doi.org/10.1080/07055900.1991.9649407.

Garrett, C., P. MacCready, and P. Rhines, 1993: Boundary Mixing and Arrested Ekman Layers: Rotating Stratified Flow Near a Sloping Boundary. *Annual Review of Fluid Mechanics*, **25 (1)**, 291–323, https://doi.org/10.1146/annurev.fl.25.010193.001451, URL http://www.annualreviews.org/doi/10.1146/annurev.fl.25.010193.001451, publisher: Annual Reviews 4139 El Camino Way, P.O. Box 10139, Palo Alto, CA 94303-0139, USA.

Garrett, C., and W. Munk, 1972: Space-Time scales of internal waves. *Geophysical Fluid Dynamics*, **3 (3)**, 225–264, https://doi.org/10.1080/03091927208236082, URL https://doi.org/10.1080/03091927208236082, publisher: Taylor & Francis _eprint: https://doi.org/10.1080/03091927208236082.

Garrett, C., and W. Munk, 1975: Space-time scales of internal waves: A progress report. *Journal of Geophysical Research (1896-1977)*, **80 (3)**, 291–297, https://doi.org/10.1029/JC080i003p00291, URL https://agupubs.onlinelibrary.wiley.com/doi/abs/10.1029/JC080i003p00291, _eprint: https://agupubs.onlinelibrary.wiley.com/doi/pdf/10.1029/JC080i003p00291.

Gregg, M., E. D'Asaro, J. Riley, and E. Kunze, 2018: Mixing Efficiency in the Ocean. *Annual Review of Marine Science*, **10 (1)**, 443–473, https://doi.org/

10.1146/annurev-marine-121916-063643, URL http://www.annualreviews.org/doi/10.1146/annurev-marine-121916-063643.

Gregg, M. C., 1989: Scaling turbulent dissipation in the thermocline. *Journal of Geophysical Research*, **94 (C7)**, 9686, https://doi.org/10.1029/JC094iC07p09686, URL http://doi.wiley.com/10.1029/JC094iC07p09686.

Gregg, M. C., T. B. Sanford, and D. P. Winkel, 2003: Reduced mixing from the breaking of internal waves in equatorial waters. *Nature*, **422 (6931)**, 513–515, https://doi.org/10.1038/nature01507, URL https://www.nature.com/articles/nature01507, number: 6931 Publisher: Nature Publishing Group.

Hamann, M. M., M. H. Alford, A. J. Lucas, A. F. Waterhouse, and G. Voet, 2021: Turbulence Driven by Reflected Internal Tides in a Supercritical Submarine Canyon. *Journal of Physical Oceanography*, **51 (2)**, 591–609, https://doi.org/10.1175/JPO-D-20-0123.1, URL https://journals.ametsoc.org/view/journals/phoc/51/2/jpo-d-20-0123.1.xml, publisher: American Meteorological Society Section: Journal of Physical Oceanography.

Henyey, F. S., J. Wright, and S. M. Flatté, 1986: Energy and action flow through the internal wave field: An eikonal approach. *Journal of Geophysical Research: Oceans*, **91 (C7)**, 8487–8495, https://doi.org/10.1029/JC091iC07p08487, URL https://agupubs.onlinelibrary.wiley.com/doi/abs/10.1029/JC091iC07p08487, _eprint: https://agupubs.onlinelibrary.wiley.com/doi/pdf/10.1029/JC091iC07p08487.

Hogg, N., P. Biscaye, W. Gardner, and W. Jr, 1982: On the Transport and Modification of Antarctic Bottom Water in the Vema Channel. *J. Mar. Res.*, **40**, 231–263.

Holmes, R. M., C. de Lavergne, and T. J. McDougall, 2019: Tracer Transport within Abyssal Mixing Layers. *Journal of Physical Oceanography*, **49 (10)**, 2669–2695, https://doi.org/10.1175/JPO-D-19-0006.1, URL https://journals.ametsoc.org/doi/full/10.1175/JPO-D-19-0006.1, publisher: American Meteorological Society.

Holmes, R. M., and T. J. McDougall, 2020: Diapycnal Transport near a Sloping Bottom Boundary. *Journal of Physical Oceanography*, **50 (11)**, 3253–3266, https://doi.org/10.1175/JPO-D-20-0066.1, URL https://journals.ametsoc.org/view/journals/phoc/50/11/jpoD200066.

xml, publisher: American Meteorological Society Section: Journal of Physical Oceanography.

Holtermann, P. L., L. Umlauf, T. Tanhua, O. Schmale, G. Rehder, and J. J. Waniek, 2012: The Baltic Sea Tracer Release Experiment: 1. Mixing rates. *Journal of Geophysical Research: Oceans*, **117 (C1)**, https://doi.org/10.1029/2011JC007439, URL https://onlinelibrary.wiley.com/doi/abs/10.1029/2011JC007439, _eprint: https://onlinelibrary.wiley.com/doi/pdf/10.1029/2011JC007439.

Hoyer, S., and J. Hamman, 2017: xarray: N-D labeled arrays and datasets in Python. *Journal of Open Research Software*, **5 (1)**, https://doi.org/10.5334/jors.148, URL http://doi.org/10.5334/jors.148.

Huang, R. X., and X. Jin, 2002: Deep Circulation in the South Atlantic Induced by Bottom-Intensified Mixing over the Midocean Ridge*. *Journal of Physical Oceanography*, **32 (4)**, 1150–1164, https://doi.org/10.1175/1520-0485(2002)032<1150:DCITSA>2.0.CO;2.

Kunze, E., E. Firing, J. M. Hummon, T. K. Chereskin, and A. M. Thurnherr, 2006: Global Abyssal Mixing Inferred from Lowered ADCP Shear and CTD Strain Profiles. *Journal of Physical Oceanography*, **36 (8)**, 1553–1576, https://doi.org/10.1175/JPO2926.1, URL https://journals.ametsoc.org/view/journals/phoc/36/8/jpo2926.1.xml, publisher: American Meteorological Society Section: Journal of Physical Oceanography.

Ledwell, J. R., T. F. Duda, M. A. Sundermeyer, and H. E. Seim, 2004: Mixing in a coastal environment: 1. A view from dye dispersion. *Journal of Geophysical Research: Oceans*, **109 (C10)**, https://doi.org/https://doi.org/10.1029/2003JC002194, URL https://agupubs.onlinelibrary.wiley.com/doi/abs/10.1029/2003JC002194, _eprint: https://agupubs.onlinelibrary.wiley.com/doi/pdf/10.1029/2003JC002194.

Ledwell, J. R., R. He, Z. Xue, S. F. DiMarco, L. J. Spencer, and P. Chapman, 2016: Dispersion of a tracer in the deep Gulf of Mexico. *Journal of Geophysical Research: Oceans*, **121 (2)**, 1110–1132, https://doi.org/https://doi.org/10.1002/2015JC011405, URL https://agupubs.onlinelibrary.wiley.com/doi/abs/10.1002/2015JC011405, _eprint: https://agupubs.onlinelibrary.wiley.com/doi/pdf/10.1002/2015JC011405.

Ledwell, J. R., and B. M. Hickey, 1995: Evidence for enhanced boundary mixing in the Santa Monica Basin. *Journal of Geophysical Research: Oceans*, **100 (C10)**, 20 665–20 679, https://doi.org/https://doi.org/10.1029/94JC01182, URL https://agupubs.onlinelibrary.wiley.com/doi/abs/10.1029/94JC01182, _eprint: https://agupubs.onlinelibrary.wiley.com/doi/pdf/10.1029/94JC01182.

Ledwell, J. R., E. T. Montgomery, K. L. Polzin, L. C. St. Laurent, R. W. Schmitt, and J. M. Toole, 2000: Evidence for enhanced mixing over rough topography in the abyssal ocean. *Nature*, **403 (6766)**, 179–182, https://doi.org/10.1038/35003164, URL http://www.nature.com/articles/35003164, publisher: Nature Publishing Group.

Ledwell, J. R., and A. J. Watson, 1991: The Santa Monica Basin tracer experiment: A study of diapycnal and isopycnal mixing. *Journal of Geophysical Research: Oceans*, **96 (C5)**, 8695–8718, https://doi.org/https://doi.org/10.1029/91JC00102, URL https://agupubs.onlinelibrary.wiley.com/doi/abs/10.1029/91JC00102, _eprint: https://agupubs.onlinelibrary.wiley.com/doi/pdf/10.1029/91JC00102.

Ledwell, J. R., A. J. Watson, and C. S. Law, 1998: Mixing of a tracer in the pycnocline. *Journal of Geophysical Research: Oceans*, **103 (C10)**, 21 499–21 529, https://doi.org/https://doi.org/10.1029/98JC01738, URL https://agupubs.onlinelibrary.wiley.com/doi/abs/10.1029/98JC01738, _eprint: https://agupubs.onlinelibrary.wiley.com/doi/pdf/10.1029/98JC01738.

Lele, R., and Coauthors, 2021: Abyssal Heat Budget in the Southwest Pacific Basin. *Journal of Physical Oceanography*, **51 (11)**, 3317–3333, https://doi.org/10.1175/JPO-D-21-0045.1, URL https://journals.ametsoc.org/view/journals/phoc/51/11/JPO-D-21-0045.1.xml, publisher: American Meteorological Society Section: Journal of Physical Oceanography.

Lumpkin, R., and K. Speer, 2007: Global Ocean Meridional Overturning. *Journal of Physical Oceanography*, **37 (10)**, 2550–2562, https://doi.org/10.1175/JPO3130.1, URL http://dx.doi.org/10.1175/JPO3130.1, iSBN: 0022-3670.

Mackay, N., J. R. Ledwell, M.-J. Messias, A. C. N. Garabato, J. A. Brearley, A. J. S. Meijers, D. C. Jones, and A. J. Watson, 2018: Diapycnal Mixing in the Southern Ocean Diagnosed Using the DIMES Tracer and Realistic Velocity Fields. *Journal of Geophysical Research: Oceans*, **123 (4)**, 2615–2634, https://doi.org/https://doi.org/10.1002/

2017JC013536, URL https://agupubs.onlinelibrary.wiley.com/doi/abs/10.1002/2017JC013536, _eprint: https://agupubs.onlinelibrary.wiley.com/doi/pdf/10.1002/2017JC013536.

MacKinnon, J. A., and Coauthors, 2017: Climate Process Team on Internal Wave–Driven Ocean Mixing. *Bulletin of the American Meteorological Society*, **98 (11)**, 2429–2454, https://doi.org/10.1175/BAMS-D-16-0030.1, URL http://journals.ametsoc.org/doi/10.1175/BAMS-D-16-0030.1.

Marshall, J., C. Hill, L. Perelman, and A. Adcroft, 1997: Hydrostatic, quasi-hydrostatic, and non-hydrostatic ocean modeling. *Journal of Geophysical Research*, **102 (C3)**, 5733, https://doi.org/10.1029/96JC02776, iSBN: 2156-2202.

Marshall, J., D. Jamous, and J. Nilsson, 1999: Reconciling thermodynamic and dynamic methods of computation of water-mass transformation rates. *Deep-Sea Research Part I: Oceanographic Research Papers*, **46 (4)**, 545–572, https://doi.org/10.1016/S0967-0637(98)00082-X, iSBN: 0967-0637.

Mashayek, A., C. P. Caulfield, and M. H. Alford, 2021: Goldilocks mixing in oceanic shear-induced turbulent overturns. *Journal of Fluid Mechanics*, **928**, https://doi.org/10.1017/jfm.2021.740, URL https://www.cambridge.org/core/journals/journal-of-fluid-mechanics/article/goldilocks-mixing-in-oceanic-shearinduced-turbulent-overturns/56115ECF93E0E3071E5C1FB119A2C479, publisher: Cambridge University Press.

Mashayek, A., R. Ferrari, S. Merrifield, J. R. Ledwell, L. St Laurent, and A. N. Garabato, 2017: Topographic enhancement of vertical turbulent mixing in the Southern Ocean. *Nature Communications*, **8**, 14 197, https://doi.org/10.1038/ncomms14197, URL http://www.nature.com/doifinder/10.1038/ncomms14197, publisher: Nature Publishing Group.

McDougall, T. J., and R. Ferrari, 2017: Abyssal Upwelling and Downwelling Driven by Near-Boundary Mixing. *Journal of Physical Oceanography*, **47 (2)**, 261–283, https://doi.org/10.1175/JPO-D-16-0082.1, URL https://journals.ametsoc.org/doi/full/10.1175/JPO-D-16-0082.1, publisher: American Meteorological Society.

McWilliams, J. C., 2016: Submesoscale currents in the ocean. *Proceedings of the Royal Society A: Mathematical, Physical and Engineering Sciences*, **472 (2189)**, 20160 117, https://doi.org/

10.1098/rspa.2016.0117, URL https://royalsocietypublishing.org/doi/10.1098/rspa.2016.0117, publisher: Royal Society.

Munk, W. H., 1966: Abyssal recipes. *Deep Sea Research and Oceanographic Abstracts*, **13 (4)**, 707–730, https://doi.org/10.1016/0011-7471(66)90602-4, arXiv: cs/9605103 ISBN: 1600117471.

Munk, W. H., and C. Wunsch, 1998: Abyssal Recipes II: energetics of tidal and wind mixing. *Deep-Sea Research Part I: Oceanographic Research Papers*, **45**, 1978–2010.

Nazarian, R. H., C. M. Burns, S. Legg, M. C. Buijsman, H. Kaur, and B. K. Arbic, 2021: On the Magnitude of Canyon-Induced Mixing. *Journal of Geophysical Research: Oceans*, **126 (11)**, e2021JC017 671, https://doi.org/10.1029/2021JC017671, URL https://onlinelibrary.wiley.com/doi/abs/10.1029/2021JC017671, _eprint: https://onlinelibrary.wiley.com/doi/pdf/10.1029/2021JC017671.

Nikurashin, M., and R. Ferrari, 2009: Radiation and Dissipation of Internal Waves Generated by Geostrophic Motions Impinging on Small-Scale Topography: Theory. *Journal of Physical Oceanography*, **40 (5)**, 1055–1074, https://doi.org/10.1175/2009JPO4199.1, URL https://journals.ametsoc.org/doi/full/10.1175/2009JPO4199.1.

Nikurashin, M., and S. Legg, 2011: A Mechanism for Local Dissipation of Internal Tides Generated at Rough Topography. *Journal of Physical Oceanography*, **41 (2)**, 378–395, https://doi.org/10.1175/2010JPO4522.1, URL http://journals.ametsoc.org/doi/abs/10.1175/2010JPO4522.1.

Osborn, T. R., 1980: Estimates of the Local Rate of Vertical Diffusion from Dissipation Measurements. *Journal of Physical Oceanography*, **10 (1)**, 83–89, https://doi.org/10.1175/1520-0485(1980)010<0083:EOTLRO>2.0.CO;2, URL http://journals.ametsoc.org/doi/abs/10.1175/1520-0485%281980%29010%3C0083%3AEOTLRO%3E2.0.CO%3B2.

Osborn, T. R., and C. S. Cox, 1972: Oceanic fine structure. *Geophysical Fluid Dynamics*, **3 (1)**, 321–345, https://doi.org/10.1080/03091927208236085, URL http://www.tandfonline.com/doi/abs/10.1080/03091927208236085.

Polzin, K., J. Toole, J. R. Ledwell, and R. Schmitt, 1997: Spatial Variability of Turbulent Mixing in the Spatial Variability Abyssal Ocean. *Science*, **276 (5309)**, 93–96, https://doi.org/10.

1126/science.276.5309.93, URL http://www.sciencemag.org/cgi/content/abstract/276/5309/93, iSBN: 0036-8075.

Polzin, K. L., 2009: An abyssal recipe. *Ocean Modelling*, **30 (4)**, 298–309, https://doi.org/10.1016/j.ocemod.2009.07.006.

Polzin, K. L., and T. J. McDougall, 2022: Chapter 7 - Mixing at the ocean's bottom boundary. *Ocean Mixing*, M. Meredith, and A. Naveira Garabato, Eds., Elsevier, 145–180, https://doi.org/10.1016/B978-0-12-821512-8.00014-1, URL https://www.sciencedirect.com/science/article/pii/B9780128215128000141.

Polzin, K. L., J. M. Toole, R. W. Schmitt, K. L. Polzin, J. M. Toole, and R. W. Schmitt, 1995: Finescale Parameterizations of Turbulent Dissipation. *Journal of Physical Oceanography*, **25 (3)**, 306–328, https://doi.org/10.1175/1520-0485(1995)025<0306:FPOTD>2.0.CO;2.

Polzin, K. L., B. Wang, Z. Wang, F. Thwaites, and A. J. Williams, 2021: Moored Flux and Dissipation Estimates from the Northern Deepwater Gulf of Mexico. *Fluids*, **6 (7)**, 237, https://doi.org/10.3390/fluids6070237, URL https://www.mdpi.com/2311-5521/6/7/237, number: 7 Publisher: Multidisciplinary Digital Publishing Institute.

Ruan, X., and J. Callies, 2020: Mixing-Driven Mean Flows and Submesoscale Eddies over Mid-Ocean Ridge Flanks and Fracture Zone Canyons. *Journal of Physical Oceanography*, **50 (1)**, 175–195, https://doi.org/10.1175/JPO-D-19-0174.1, URL https://journals.ametsoc.org/view/journals/phoc/50/1/jpo-d-19-0174.1.xml, publisher: American Meteorological Society Section: Journal of Physical Oceanography.

Ruan, X., and R. Ferrari, 2021: Diagnosing Diapycnal Mixing from Passive Tracers. *Journal of Physical Oceanography*, **51 (3)**, 757–767, https://doi.org/10.1175/JPO-D-20-0194.1, URL https://journals.ametsoc.org/view/journals/phoc/51/3/JPO-D-20-0194.1.xml, publisher: American Meteorological Society Section: Journal of Physical Oceanography.

Simmons, H. L., S. R. Jayne, L. C. St. Laurent, and A. J. Weaver, 2004: Tidally driven mixing in a numerical model of the ocean general circulation. *Ocean Modelling*, **6 (3-4)**, 245–263, https://doi.org/10.1016/S1463-5003(03)00011-8, iSBN: 1463-5003.

Spingys, C. P., A. C. N. Garabato, S. Legg, K. L. Polzin, E. P. Abrahamsen, C. E. Buckingham, A. Forryan, and E. E. Frajka-Williams, 2021: Mixing and Transformation in a Deep Western Boundary Current: A Case Study. *Journal of Physical Oceanography*, **51 (4)**, 1205–1222, https://doi.org/10.1175/JPO-D-20-0132.1, URL https://journals.ametsoc.org/view/journals/phoc/aop/JPO-D-20-0132.1/JPO-D-20-0132.1.xml, publisher: American Meteorological Society Section: Journal of Physical Oceanography.

St. Laurent, L., and R. W. Schmitt, 1999: The Contribution of Salt Fingers to Vertical Mixing in the North Atlantic Tracer Release Experiment. *Journal of Physical Oceanography*, **29 (7)**, 1404–1424, https://doi.org/10.1175/1520-0485(1999)029<1404:TCOSFT>2.0.CO;2, URL https://journals.ametsoc.org/view/journals/phoc/29/7/1520-0485_1999_029_1404_tcosft_2.0.co_2.xml, publisher: American Meteorological Society Section: Journal of Physical Oceanography.

St. Laurent, L. C., J. M. Toole, and R. W. Schmitt, 2001: Buoyancy Forcing by Turbulence above Rough Topography in the Abyssal Brazil Basin*. *Journal of Physical Oceanography*, **31 (12)**, 3476–3495, https://doi.org/10.1175/1520-0485(2001)031<3476:BFBTAR>2.0.CO;2.

Stommel, H., and A. B. Arons, 1959: On the abyssal circulation of the world ocean — II. An idealized model of the circulation pattern and amplitude in oceanic basins. *Deep Sea Research (1953)*, **6**, 217–233, https://doi.org/10.1016/0146-6313(59)90075-9, URL http://www.sciencedirect.com/science/article/pii/0146631359900759.

Sundermeyer, M. A., E. A. Terray, J. R. Ledwell, A. G. Cunningham, P. E. LaRocque, J. Banic, and W. J. Lillycrop, 2007: Three-Dimensional Mapping of Fluorescent Dye Using a Scanning, Depth-Resolving Airborne Lidar. *Journal of Atmospheric and Oceanic Technology*, **24 (6)**, 1050–1065, https://doi.org/10.1175/JTECH2027.1, URL https://journals.ametsoc.org/view/journals/atot/24/6/jtech2027_1.xml, publisher: American Meteorological Society Section: Journal of Atmospheric and Oceanic Technology.

Talley, L. D., 2013: Closure of the Global Overturning Circulation Through the Indian, Pacific, and Southern Oceans: Schematics and Transports. *Oceanography*, **26 (1)**, 80–97, https://doi.org/10.5670/oceanog.2013.07, URL http://apps.webofknowledge.com/full_record.do?product=UA&

search_mode=GeneralSearch&qid=14&SID=W1jPgx8kkS6brME6NvD&page=1&doc=1, arXiv: 1011.1669v3 ISBN: 1042-8275.

Taylor, G. I., 1922: Diffusion by Continuous Movements. *Proceedings of the London Mathematical Society*, **s2-20 (1)**, 196–212, https://doi.org/https://doi.org/10.1112/plms/s2-20.1.196, URL https://londmathsoc.onlinelibrary.wiley.com/doi/abs/10.1112/plms/s2-20.1.196, _eprint: https://londmathsoc.onlinelibrary.wiley.com/doi/pdf/10.1112/plms/s2-20.1.196.

Taylor, G. I., 1953: Dispersion of soluble matter in solvent flowing slowly through a tube. *Proceedings of the Royal Society of London. Series A. Mathematical and Physical Sciences*, **219 (1137)**, 186–203, https://doi.org/10.1098/rspa.1953.0139, URL https://royalsocietypublishing.org/doi/10.1098/rspa.1953.0139, publisher: Royal Society.

Taylor, J. R., S. M. d. B. Kops, C. P. Caulfield, and P. F. Linden, 2019: Testing the Assumptions Underlying Ocean Mixing Methodologies Using Direct Numerical Simulations. *Journal of Physical Oceanography*, **49 (11)**, 2761–2779, https://doi.org/10.1175/JPO-D-19-0033.1, URL https://journals.ametsoc.org/view/journals/phoc/49/11/jpo-d-19-0033.1.xml, publisher: American Meteorological Society Section: Journal of Physical Oceanography.

Thorpe, S. A., and G. E. R. Deacon, 1977: Turbulence and mixing in a Scottish Loch. *Philosophical Transactions of the Royal Society of London. Series A, Mathematical and Physical Sciences*, **286 (1334)**, 125–181, https://doi.org/10.1098/rsta.1977.0112, URL https://royalsocietypublishing.org/doi/10.1098/rsta.1977.0112, publisher: Royal Society.

Thurnherr, A. M., L. Clément, L. S. Laurent, R. Ferrari, and T. Ijichi, 2020: Transformation and Upwelling of Bottom Water in Fracture Zone Valleys. *Journal of Physical Oceanography*, **50 (3)**, 715–726, https://doi.org/10.1175/JPO-D-19-0021.1, URL https://journals.ametsoc.org/view/journals/phoc/50/3/jpo-d-19-0021.1.xml, publisher: American Meteorological Society Section: Journal of Physical Oceanography.

Thurnherr, A. M., and Coauthors, 2005: Mixing Associated with Sills in a Canyon on the Midocean Ridge Flank*. *Journal of Physical Oceanography*, **35 (8)**, 1370–1381, https://doi.org/10.1175/JPO2773.1, URL http://journals.ametsoc.org/doi/abs/10.1175/JPO2773.1.

Tozer, B., D. T. Sandwell, W. H. F. Smith, C. Olson, J. R. Beale, and P. Wessel, 2019: Global Bathymetry and Topography at 15 Arc Sec: SRTM15+. *Earth and Space Science*, **6 (10)**, 1847–1864, https://doi.org/10.1029/2019EA000658, URL https://agupubs.onlinelibrary.wiley.com/doi/abs/10.1029/2019EA000658, _eprint: https://agupubs.onlinelibrary.wiley.com/doi/pdf/10.1029/2019EA000658.

Trossman, D., and Coauthors, 2020: Tracer and observationally-derived constraints on horizontal and diapycnal diffusivities in ocean models. URL http://www.essoar.org/doi/10.1002/essoar.10502123.4, archive Location: world Publisher: Earth and Space Science Open Archive Section: Oceanography, https://doi.org/10.1002/essoar.10502123.4.

Tulloch, R., and Coauthors, 2014: Direct Estimate of Lateral Eddy Diffusivity Upstream of Drake Passage. *Journal of Physical Oceanography*, **44 (10)**, 2593–2616, https://doi.org/10.1175/JPO-D-13-0120.1, URL https://journals.ametsoc.org/view/journals/phoc/44/10/jpo-d-13-0120.1.xml, publisher: American Meteorological Society Section: Journal of Physical Oceanography.

Visbeck, M., M. Dengler, T. S. Tanhua, and M. Freund, 2020: Mixing and Upwelling Dynamics along the Continental Slope off Peru inferred from Tracer Release, Hydrographic and Microstructure Measurements. AGU, URL https://agu.confex.com/agu/osm20/meetingapp.cgi/Paper/651229.

Wagner, G. L., G. Flierl, R. Ferrari, G. Voet, G. S. Carter, M. H. Alford, and J. B. Girton, 2019: Squeeze Dispersion and the Effective Diapycnal Diffusivity of Oceanic Tracers. *Geophysical Research Letters*, **46 (10)**, 5378–5386, https://doi.org/10.1029/2019GL082458, URL https://onlinelibrary.wiley.com/doi/abs/10.1029/2019GL082458, _eprint: https://onlinelibrary.wiley.com/doi/pdf/10.1029/2019GL082458.

Walin, G., 1982: On the relation between sea-surface heat flow and thermal circulation in the ocean. *Tellus*, **34 (2)**, 187–195, https://doi.org/10.3402/tellusa.v34i2.10801, URL https://doi.org/10.3402/tellusa.v34i2.10801.

Waterhouse, A. F., and Coauthors, 2014: Global Patterns of Diapycnal Mixing from Measurements of the Turbulent Dissipation Rate. *Journal of Physical Oceanography*, **44 (7)**, 1854–1872, https://doi.org/10.1175/JPO-D-13-0104.1, URL http://journals.ametsoc.org/doi/abs/10.1175/JPO-D-13-0104.1, iSBN: 0022-3670.

Watson, A. J., J. R. Ledwell, M.-J. Messias, B. A. King, N. Mackay, M. P. Meredith, B. Mills, and A. C. Naveira Garabato, 2013: Rapid cross-density ocean mixing at mid-depths in the Drake Passage measured by tracer release. *Nature*, **501 (7467)**, 408–411, https://doi.org/10.1038/nature12432, URL http://www.nature.com/articles/nature12432, publisher: Nature Publishing Group.

Watson, A. J., J. R. Ledwell, D. J. Webb, and C. Wunsch, 1988: Purposefully Released Tracers [and Discussion]. *Philosophical Transactions of the Royal Society of London. Series A, Mathematical and Physical Sciences*, **325 (1583)**, 189–200, URL https://www.jstor.org/stable/38109, publisher: The Royal Society.

Wenegrat, J. O., J. Callies, and L. N. Thomas, 2018: Submesoscale Baroclinic Instability in the Bottom Boundary Layer. *Journal of Physical Oceanography*, JPO–D–17–0264.1, https://doi.org/10.1175/JPO-D-17-0264.1, URL http://journals.ametsoc.org/doi/10.1175/JPO-D-17-0264.1.

Whalen, C. B., 2021: Best Practices for Comparing Ocean Turbulence Measurements across Spatiotemporal Scales. *Journal of Atmospheric and Oceanic Technology*, **38 (4)**, 837–841, https://doi.org/10.1175/JTECH-D-20-0175.1, URL https://journals.ametsoc.org/view/journals/atot/38/4/JTECH-D-20-0175.1.xml, publisher: American Meteorological Society Section: Journal of Atmospheric and Oceanic Technology.

Whalen, C. B., C. de Lavergne, A. C. Naveira Garabato, J. M. Klymak, J. A. MacKinnon, and K. L. Sheen, 2020: Internal wave-driven mixing: governing processes and consequences for climate. *Nature Reviews Earth & Environment*, **1 (11)**, 606–621, https://doi.org/10.1038/s43017-020-0097-z, URL https://www.nature.com/articles/s43017-020-0097-z, number: 11 Publisher: Nature Publishing Group.